

# Error estimates for the Scaled Boundary Finite Element Method

Karolinne O. Coelho<sup>a,\*</sup>, Philippe R. B. Devloo<sup>a</sup>, Sônia M. Gomes<sup>b</sup>

<sup>a</sup> *FEC - Universidade Estadual de Campinas, R. Josiah Willard Gibbs 85 - Cidade Universitária, Campinas, SP, CEP 13083-839, Brazil*

<sup>b</sup> *IMECC - Universidade Estadual de Campinas, Campinas, SP, Brazil*

---

## Abstract

The Scaled Boundary Finite Element Method (SBFEM) is a technique in which approximation spaces are constructed using a semi-analytical approach. They are based on partitions of the computational domain by polygonal/polyhedral subregions, where the shape functions approximate local Dirichlet problems with piecewise polynomial trace data. Using this operator adaptation approach, and by imposing a starlike scaling requirement on the subregions, the representation of local SBFEM shape functions in radial and surface directions are obtained from eigenvalues and eigenfunctions of an ODE system, whose coefficients are determined by the element geometry and the trace polynomial spaces. The aim of this paper is to derive a priori error estimates for SBFEM's solutions of harmonic test problems. For that, the SBFEM spaces are characterized in the context of Duffy's approximations for which a gradient-orthogonality constraint is imposed. As a consequence, the scaled boundary functions are gradient-orthogonal to any function in Duffy's spaces vanishing at the mesh skeleton, a mimetic version of a well-known property valid for harmonic functions. This orthogonality property is applied to provide a priori SBFEM error estimates in terms of known finite element interpolant errors of the exact solution. Similarities with virtual harmonic approximations are also explored for the understanding of SBFEM convergence properties. Numerical experiments with 2D and 3D polytopal meshes confirm optimal SBFEM convergence rates for two test problems with smooth solutions. Attention is also paid to the approximation of a point singular solution by using SBFEM close to the singularity and finite element approximations elsewhere, revealing optimal accuracy rates of standard regular contexts.

*Keywords:* Scaled boundary finite element method, a priori error estimates, Duffy's approximations

---

## 1. Introduction

The Scaled Boundary Finite Element Method (SBFEM) is a Galerkin method in which the approximation spaces are constructed using a semi-analytical approach [1, 2, 3, 4]. They are based on general partitions of the computational domain by polygonal/polyhedral subregions  $S$  (called  $S$ -elements), which are supposed to verify the starlike scaling requirement such that any point on the boundary  $\partial S$  can be directly visible from a center point (scaling center). The shape functions are computed by the application of the scaled boundary technique, involving a specific parametrization of the  $S$ -elements,

---

\*Corresponding author - Phone +55 19 3521-1149

*Email addresses:* karolinneoc@gmail.com (Karolinne O. Coelho), phil@fec.unicamp.br (Philippe R. B. Devloo), soniag@unicamp.br (Sônia M. Gomes)

which is possible thanks to their scaling property. In classical FE methods, the local approximations are (mapped) polynomials, and these are known to fail or have very low convergence rates when the exact solutions can not be properly represented by polynomials. In SBFEM, discretization by piecewise polynomials only takes place at  $\partial S$ , whilst the functions are constructed by approximating local Dirichlet problems internally to  $S$ . The method is discussed in the books [3, 4], and articles therein cited.

This incorporation of analytic knowledge about the local behavior of the exact solution in the approximation spaces is the main property of SBFEM. Therefore, it can be viewed as an operator adapted method. As discussed in [5, 6], in the context of the Partition of Unity Method, these methods can be expected to perform better when compared with standard polynomial based FE approximations. They reduce the number of degrees of freedom significantly and hence the computational cost, while improving the quality of the solutions. For the case of SBFEM, where only boundary values of the subdomains are discretized by local surface polynomials, its operator adapted approach revealed itself to be particularly efficient to approximate problems with stress singularities, such as crack tips, v-notches, and re-entrant corners to name a few applications in elasticity [7, 8, 9, 10, 11]. More recently, the method has been applied to highly irregular and heterogeneous domains due to the flexibility in generating SBFEM meshes [12, 13]. For instance, the SBFEM has been applied in quadtree and octree meshes since hanging nodes can be avoided due to the flexible topology of SBFEM polygonal/polyhedral subregions [14, 15, 10].

The aim of this paper is to derive a priori error estimates of SBFEM approximations for the case of Laplace’s equation. Although numerical experiments in the literature point that optimal rates of convergence are obtained using SBFEM approximations [16, 17], the mathematical demonstrations that give support to the observed numerical results are new contributions of the current work. For that, we explore two different aspects of SBFEM spaces, shared with Duffy’s approximations [18] or with virtual harmonic spaces [19].

Taking advantage of the scaling property, functions can be represented in the  $S$ -elements by coordinates in radial and surface directions. Their values on the boundary  $\partial S$  live in piecewise polynomial trace spaces, which are radially extended to the interior of the subdomain. Therefore, this property puts SBFEM’s spaces in the context of Duffy’s approximations [18], whose definitions are summarized in Section 2. Partitions of  $S$  are obtained by a geometric transformation collapsing a reference quadrilateral, hexahedron or prism on triangular, pyramidal or tetrahedral elements  $K \subset S$ , each one sharing the scaling center as a vertex (see Section 3.2).

For the model Laplace problem under consideration, the focus of the SBFEM operator adapted approach is the approximations inside  $S$ -elements by “radial harmonic extensions” of surface components. It is shown that SBFEM’s spaces are Duffy’s approximations constructed to solve Laplace problems with piecewise polynomial Dirichlet data over  $\partial S$ . SBFEM spaces are characterized by the enforcement of a gradient-orthogonality constraint with respect to Duffy’s approximations vanishing on  $\partial S$  and at the center point, as demonstrated in Section 3.3. This perspective on SBFEM approximations reveals that the local scaled boundary shape functions are constructed based on an orthogonality condition. By enforcing these intrinsic orthogonality constraints, their parametrization in radial and surface directions emerge from the eigenvalues and eigenfunctions of an ODE system, whose coefficients are determined by the element geometry and the trace polynomial spaces. The scaled boundary functions are gradient-orthogonal to an extended class of Duffy’s functions that vanish at the mesh skeleton. It can be viewed as a mimetic version of a well-known property valid for harmonic functions. These aspects are stated

in Proposition 3.1 and used as a key tool to the development of energy error estimates for the SBFEM in terms of FE interpolation errors in Section 5, as shown in Theorem 5.1, one of the main contributions of this study.

SBFEM also has close similarities with virtual harmonic approximation spaces recently introduced in [19], as explored in Section 4.3 and summarized in Theorem 5.2. In both cases the trace functions are piecewise polynomials defined over subregion boundaries  $\partial S$ , which are extended to the interior of  $S$  by solving local Dirichlet Laplace problems: whilst the functions in the local virtual spaces are strongly harmonic, in SBFEM spaces this property is enforced in a reduced extent. Thus, SBFEM approximation errors may come from the trace polynomial interpolation or by their deviation of being harmonic. However, unlike for the virtual harmonic subspaces, it is possible to explore the radial Duffy's structure to explicitly compute SBFEM shape functions.

In Section 6, we present results of SBFEM computational simulations for some harmonic test problems confirming the predicted theoretical convergence results of Section 5. We consider 2D and 3D cases with smooth solutions, and discretizations based on different  $S$ -partition geometry, which are formed by internally collapsed triangular, pyramidal, or tetrahedral elements. In the same section, we present  $p$ -convergence histories verifying asymptotic exponential convergence rates in terms of degrees of freedom (DOF), and compare results with respect to the ones given by usual FE methods based on partitions obtained by the conglomeration of the internal collapsed elements. We also pay attention to the approximation of a singular problem where the singularity occurs by the change of boundary condition and observe that optimal rates of convergence holds using few DOF, using SBFEM to resolve the singularity. We draw some concluding remarks in Section 7.

## 2. Duffy's approximations in triangles, pyramids and tetrahedra

Duffy's transformations [18] (also referred to as collapsed coordinate systems) are invertible maps of a rectangle into a triangle, a hexahedron to a pyramid, or a prism to a tetrahedron. These maps were originally proposed for integration of vertex singularities and they are widely applied to define integration quadrature formulae in triangles [20, 21]. Duffy's transformations are also the basic tools for the construction of spectral methods on simplices (triangles, tetrahedra) [22]. Collapsed isoparametric elements parametrized by Duffy's transformations also have applications in crack problems [23, 24, 25].

### 2.1. Duffy's geometric transformations

The master elements to be considered have the general form  $\hat{K} = [0, 1] \times \hat{L} \subset \mathbb{R}^d$ , where  $\hat{L} \subset \mathbb{R}^{d-1}$ ,  $d = 2, 3$ . In the parametric coordinates  $\hat{\mathbf{x}} = (\xi, \boldsymbol{\eta}) \in \hat{K}$ ,  $\xi$  plays the role of radial variable, and  $\boldsymbol{\eta}$  refers to surface coordinates. The geometry of the master elements may be one of the following kinds:

- Rectangle  $\hat{K}$ , where  $\hat{L} = \hat{I}$  is the interval  $\hat{I} = [-1, 1]$ .
- Hexahedron  $\hat{K}$ , where  $\hat{L} = \hat{Q}$  is the rectangle  $\hat{Q} = [-1, 1] \times [-1, 1]$ .
- Prism  $\hat{K}$ , where  $\hat{L} = \hat{T}$  is the triangle  $\hat{T} = \{\boldsymbol{\eta} = (\eta_1, \eta_2); 0 \leq \eta_i \leq 1, \eta_1 + \eta_2 \leq 1\}$ .

The key aspect of geometric Duffy's transformations  $F_K : \hat{K} \rightarrow K$  is the collapse of one facet in  $\hat{K}$  on a single vertex of the deformed element  $K$ . These maps are also referred in

the literature as collapsed coordinate systems [22]. If  $\mathbf{x}$  denotes the Cartesian coordinate in  $K$ , the mapped points  $\mathbf{x} = F_K(\xi, \boldsymbol{\eta}) \in K$  are generically defined by

$$F_K(\xi, \boldsymbol{\eta}) = \xi (F_L(\boldsymbol{\eta}) - \mathbf{a}_0) + \mathbf{a}_0, \quad (1)$$

where  $\mathbf{a}_0$  is a vertex in  $K$ , and  $L \subset \partial K$  refers to a facet opposite to  $\mathbf{a}_0$ , which is supposed to be mapped by the geometric transformation  $F_L : \hat{L} \rightarrow L$ . Notice that the whole facet  $\{(0, \boldsymbol{\eta}), \boldsymbol{\eta} \in \hat{L}\} \subset \hat{K}$  is collapsed over the vertex  $\mathbf{a}_0 \in K$ , so that  $K$  can be regarded as a quadrilateral with two identical vertices, a hexahedron with four equal vertices, or a prism with three identical vertices. That is why  $\mathbf{a}_0$  is called the collapsed vertex. The mapping  $F_K$  can also be seen as a scaling from a point  $F_L(\boldsymbol{\eta}) \in L$  to the vertex  $\mathbf{a}_0$ . This process generates radial lines  $[\mathbf{a}_0, F_L(\boldsymbol{\eta})] = \mathbf{a}_0 + \xi \mathbf{r}(\boldsymbol{\eta})$ , where  $\mathbf{r}(\boldsymbol{\eta}) = F_L(\boldsymbol{\eta}) - \mathbf{a}_0$ .

The Jacobian matrix  $\mathbf{J}_K = \nabla_{\hat{\mathbf{x}}} F_K$  of the transformation (1) is

$$\mathbf{J}_K(\xi, \boldsymbol{\eta}) = [F_L(\boldsymbol{\eta}) - \mathbf{a}_0 \quad \xi \nabla_{\boldsymbol{\eta}} F_L(\boldsymbol{\eta})] = \mathbf{J}_K(1, \boldsymbol{\eta}) \begin{bmatrix} 1 & 0 \\ 0 & \xi \mathbf{I}_{d-1} \end{bmatrix}, \quad (2)$$

where  $\mathbf{I}_{d-1}$  is the  $d-1 \times d-1$  identity matrix, and  $\mathbf{J}_K(1, \boldsymbol{\eta}) = [F_L(\boldsymbol{\eta}) - \mathbf{a}_0 \quad \nabla_{\boldsymbol{\eta}} F_L(\boldsymbol{\eta})]$  is the Jacobian matrix at the surface points where  $F_K(1, \boldsymbol{\eta}) = F_L(\boldsymbol{\eta})$ . Thus

$$\mathbf{J}_K^{-1} = \begin{pmatrix} 1 & 0 \\ 0 & \frac{1}{\xi} \mathbf{I}_{d-1} \end{pmatrix} \mathbf{J}_K(1, \boldsymbol{\eta})^{-1}. \quad (3)$$

In the following, the geometric transformation (1) is illustrated for the three different element geometries considered in the current study.

*Case 1: quadrilateral  $\hat{K}$  to triangular  $K$*

Let  $\hat{K}$  be the rectangular master element with vertices listed in the next table

$\hat{\mathbf{a}}_0$	$\hat{\mathbf{a}}_1$	$\hat{\mathbf{a}}_2$	$\hat{\mathbf{a}}_3$
$(0, -1)$	$(1, -1)$	$(1, 1)$	$(0, 1)$

and consider a general triangular element, with vertices  $\mathbf{a}_0 = F_K(\hat{\mathbf{a}}_0)$ ,  $\mathbf{a}_1 = F_K(\hat{\mathbf{a}}_1)$ , and  $\mathbf{a}_2 = F_K(\hat{\mathbf{a}}_2)$ , as illustrated in Figure 1. Notice that the edge  $[\hat{\mathbf{a}}_0, \hat{\mathbf{a}}_3]$  collapses onto the vertex  $\mathbf{a}_0 = F_K(\hat{\mathbf{a}}_0) \in K$ , whilst  $\mathbf{a}_1$  and  $\mathbf{a}_2$  are the vertices of the opposite edge  $L = F_K(1, \boldsymbol{\eta}) = F_L(\boldsymbol{\eta})$ .

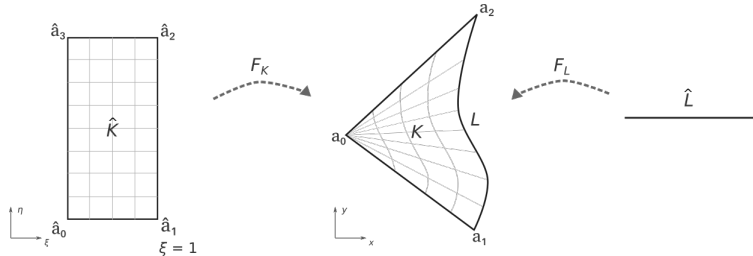


Figure 1: Geometric illustration of Duffy's transformation over a triangle as a collapsed quadrilateral.

*Case 2: hexahedral  $\hat{K}$  to pyramidal  $K$*

The master element is the hexahedron  $\hat{K}$  whose vertices are listed bellow.

$\hat{\mathbf{a}}_0$	$\hat{\mathbf{a}}_1$	$\hat{\mathbf{a}}_2$	$\hat{\mathbf{a}}_3$	$\hat{\mathbf{a}}_4$	$\hat{\mathbf{a}}_5$	$\hat{\mathbf{a}}_6$	$\hat{\mathbf{a}}_7$
$(0, -1, -1)$	$(1, -1, -1)$	$(1, 1, -1)$	$(1, 1, 1)$	$(1, -1, 1)$	$(0, -1, 1)$	$(0, 1, 1)$	$(0, 1, -1)$

Figure 2 illustrates a mapped pyramid with vertices  $\mathbf{a}_i = F_K(\hat{\mathbf{a}}_i)$ ,  $i = 0, \dots, 4$ ,  $\mathbf{a}_0$  being the collapsed vertex with opposite quadrilateral face  $L = [\mathbf{a}_1, \mathbf{a}_2, \mathbf{a}_3, \mathbf{a}_4]$ . Observe that:

1. The rectangular face  $[\hat{\mathbf{a}}_0, \hat{\mathbf{a}}_5, \hat{\mathbf{a}}_6, \hat{\mathbf{a}}_7]$  collapses onto  $\mathbf{a}_0$ ;
2. The face  $[\hat{\mathbf{a}}_0, \hat{\mathbf{a}}_1, \hat{\mathbf{a}}_4, \hat{\mathbf{a}}_5]$  collapses onto the triangle  $[\mathbf{a}_0, \mathbf{a}_1, \mathbf{a}_4]$ ;
3. The face  $[\hat{\mathbf{a}}_0, \hat{\mathbf{a}}_1, \hat{\mathbf{a}}_2, \hat{\mathbf{a}}_7]$  collapses onto the triangle  $[\mathbf{a}_0, \mathbf{a}_1, \mathbf{a}_2]$ ;
4. The face  $[\hat{\mathbf{a}}_2, \hat{\mathbf{a}}_3, \hat{\mathbf{a}}_6, \hat{\mathbf{a}}_7]$  collapses onto the triangle  $[\mathbf{a}_0, \mathbf{a}_2, \mathbf{a}_3]$ ;
5. The face  $[\hat{\mathbf{a}}_3, \hat{\mathbf{a}}_6, \hat{\mathbf{a}}_5, \hat{\mathbf{a}}_4]$  collapses onto the triangle  $[\mathbf{a}_0, \mathbf{a}_4, \mathbf{a}_3]$ .

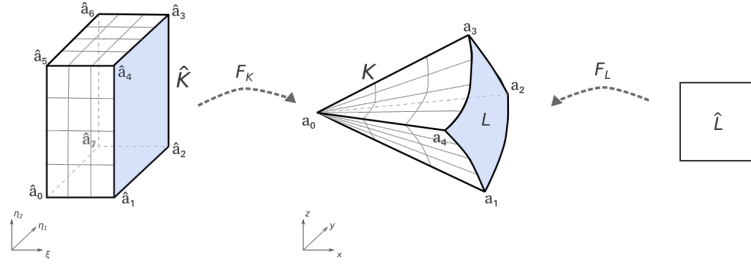


Figure 2: Geometric illustration of a Duffy's transformation over a pyramid as a collapsed hexahedron.

*Case 3: prismatic  $\hat{K}$  to tetrahedral  $K$*

The master element is the prism  $\hat{K}$  whose vertices are listed bellow.

$\hat{\mathbf{a}}_0$	$\hat{\mathbf{a}}_1$	$\hat{\mathbf{a}}_2$	$\hat{\mathbf{a}}_3$	$\hat{\mathbf{a}}_4$	$\hat{\mathbf{a}}_5$
$(0, 0, 0)$	$(1, 1, 0)$	$(0, 1, 0)$	$(0, 1, 1)$	$(1, 0, 0)$	$(0, 0, 1)$

In the tetrahedron shown in Figure 3, with vertices  $\mathbf{a}_i = F_K(\hat{\mathbf{a}}_i)$ ,  $i = 0, \dots, 3$ , the collapsed vertex is  $\mathbf{a}_0$  and the opposite quadrilateral face is  $L = [\mathbf{a}_1, \mathbf{a}_2, \mathbf{a}_3]$ . Note that:

1. The triangular face  $[\hat{\mathbf{a}}_0, \hat{\mathbf{a}}_4, \hat{\mathbf{a}}_5]$  collapses onto the vertex  $\mathbf{a}_0$ ;
2. The quadrilateral face  $[\hat{\mathbf{a}}_0, \hat{\mathbf{a}}_4, \hat{\mathbf{a}}_2, \hat{\mathbf{a}}_3]$  collapses onto the triangle  $[\mathbf{a}_0, \mathbf{a}_2, \mathbf{a}_3]$ ;
3. The quadrilateral face  $[\hat{\mathbf{a}}_0, \hat{\mathbf{a}}_3, \hat{\mathbf{a}}_1, \hat{\mathbf{a}}_5]$  collapses onto the triangle  $[\mathbf{a}_0, \mathbf{a}_1, \mathbf{a}_3]$ ;
4. The quadrilateral face  $[\hat{\mathbf{a}}_1, \hat{\mathbf{a}}_2, \hat{\mathbf{a}}_4, \hat{\mathbf{a}}_5]$  collapses onto the triangle  $[\mathbf{a}_0, \mathbf{a}_1, \mathbf{a}_2]$ .

We recall that a hexahedron to tetrahedron Duffy's transformation can also be derived, as adopted in [22], first via a preliminary step hexahedron to prism, and then the prism to tetrahedron described above.

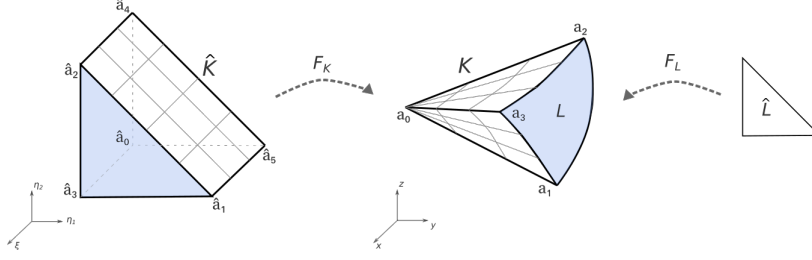


Figure 3: Geometric illustration of a Duffy's transformation over a tetrahedron as a collapsed prism.

## 2.2. Duffy's approximations

Duffy's approximations refer to functions  $\phi = \mathbb{F}_K(\hat{\phi})$  defined in  $K$  and obtained backtracking functions  $\hat{\phi}(\xi, \boldsymbol{\eta})$  defined in  $\hat{K}$ , meaning that

$$\phi(\mathbf{x}) = \hat{\phi}(\xi, \boldsymbol{\eta}), \quad \text{for } \mathbf{x} = F_K(\xi, \boldsymbol{\eta}) \in K.$$

The focus of this paper is on functions  $\phi$  obtained by separating variables in  $\hat{\phi}(\xi, \boldsymbol{\eta}) = \hat{\rho}(\xi)\hat{\alpha}(\boldsymbol{\eta})$ , where  $\hat{\rho}(\xi)$  is called the radial component, and  $\hat{\alpha}(\boldsymbol{\eta})$  is the surface component. It is clear that constant functions in  $\hat{K}$  are mapped to constant functions in  $K$ . It should also be noted that for the cases where  $\hat{\alpha}(\boldsymbol{\eta})$  is not a constant function, the well definition of  $\phi$  at the collapsed point  $\mathbf{a}_0$  requires that  $\hat{\rho}(0) = 0$ , so that  $\phi(\mathbf{a}_0) = 0$ .

We consider function spaces

$$\mathcal{D}_k(\hat{K}) = \{\hat{\phi}(\xi, \boldsymbol{\eta}) = \hat{\rho}(\xi)\hat{\alpha}(\boldsymbol{\eta}); \hat{\alpha}(\boldsymbol{\eta}) \in V_k(\hat{L}),$$

where the surface components  $\hat{\alpha}(\boldsymbol{\eta}) \in V_k(\hat{L})$  used to define FE approximation spaces  $V_k(L) = \mathbb{F}_L(V_k(\hat{L}))$ , are finite dimensional polynomial spaces  $V_k(\hat{L})$ . The following cases shall be studied:

1.  $V_k(\hat{L}) = \mathbb{P}_k(\hat{L})$ , polynomials of total degree not greater than  $k$ , for the interval  $\hat{L} = [-1, 1]$  or for the triangle  $\hat{L} = \hat{T}$ .
2.  $V_k(\hat{L}) = \mathbb{Q}_{k,k}(\hat{L})$ , polynomials of degree not greater than  $k$  on each coordinate  $\eta_1, \eta_2$ , for the quadrilateral  $\hat{L} = \hat{Q}$ .

### Gradient operation in $\mathcal{D}_k(K)$

We restrict the study to mapped spaces  $\mathcal{D}_k(K) = \mathbb{F}_K(\mathcal{D}_k(\hat{K})) \subset H^1(K)$ . For instance, as already observed in [26] for the case of triangular elements  $K$ ,  $H^1(K)$  corresponds to  $H_\omega^1(\hat{K})$  where  $H_\omega^1(\hat{K}) := \{\hat{\phi} \in L_\omega^2(\hat{K}) : \partial_{\boldsymbol{\eta}} \hat{\phi} \in L_{\omega^{-1}}^2(\hat{K}) \text{ and } \partial_\xi \hat{\phi} \in L_\omega^2(\hat{K})\}$ , where  $\omega(\xi, \boldsymbol{\eta}) = \xi |\mathbf{J}_K(1, \boldsymbol{\eta})|$ . Particularly,  $\partial_{\boldsymbol{\eta}} \hat{\phi}(0, \boldsymbol{\eta}) = 0$  for bounded  $\partial_y \phi(x, y)$ .

The chain rule implies that

$$\begin{aligned} \nabla_{\mathbf{x}} \phi(\mathbf{x}) &= [\mathbf{J}_K(1, \boldsymbol{\eta})]^{-T} \begin{bmatrix} 1 & 0 \\ 0 & \frac{1}{\xi} \mathbf{I}_{d-1} \end{bmatrix} \begin{bmatrix} \hat{\rho}'(\xi) \hat{\alpha}(\boldsymbol{\eta}) \\ \hat{\rho}(\xi) \nabla_{\boldsymbol{\eta}} \hat{\alpha}(\boldsymbol{\eta}) \end{bmatrix} \\ &= [\mathbf{J}_K(1, \boldsymbol{\eta})]^{-T} \begin{bmatrix} \hat{\rho}'(\xi) \hat{\alpha}(\boldsymbol{\eta}) \\ \frac{1}{\xi} \hat{\rho}(\xi) \nabla_{\boldsymbol{\eta}} \hat{\alpha}(\boldsymbol{\eta}) \end{bmatrix} = [\mathbf{J}_K(1, \boldsymbol{\eta})]^{-T} \begin{bmatrix} \hat{\alpha}(\boldsymbol{\eta}) & 0 \\ 0 & \nabla_{\boldsymbol{\eta}} \hat{\alpha}(\boldsymbol{\eta}) \end{bmatrix} \begin{bmatrix} \hat{\rho}'(\xi) \\ \frac{1}{\xi} \hat{\rho}(\xi) \end{bmatrix}. \end{aligned} \quad (4)$$

If  $\hat{\alpha}(\boldsymbol{\eta}) = \sum_l \alpha^l \hat{N}_k^l(\boldsymbol{\eta})$  is a linear combination of FE shape functions  $\hat{N}_k^l(\boldsymbol{\eta})$  forming a basis for  $V_k(\hat{L})$ , then

$$\nabla_{\mathbf{x}} \phi(\mathbf{x}) = \sum_l \alpha^l \begin{bmatrix} \underline{B}_{1l}(\boldsymbol{\eta}) & \underline{B}_{2l}(\boldsymbol{\eta}) \end{bmatrix} \begin{bmatrix} \hat{\rho}'(\xi) \\ \frac{1}{\xi} \hat{\rho}(\xi) \end{bmatrix}, \quad (5)$$

where

$$\underline{B}_{1l}(\boldsymbol{\eta}) = [\mathbf{J}_K(1, \boldsymbol{\eta})]^{-T} \begin{bmatrix} \hat{N}_k^l(\boldsymbol{\eta}) \\ 0 \end{bmatrix}, \text{ and } \underline{B}_{2l}(\boldsymbol{\eta}) = [\mathbf{J}_K(1, \boldsymbol{\eta})]^{-T} \begin{bmatrix} 0 \\ \nabla_{\boldsymbol{\eta}} \hat{N}_k^l(\boldsymbol{\eta}) \end{bmatrix}. \quad (6)$$

*Special case:*  $\hat{\alpha}(\boldsymbol{\eta}) \equiv 1$

Let us consider the particular cases of  $\phi(\mathbf{x}) \in \mathcal{D}_k(K)$ , for which  $\hat{\phi}(\xi, \boldsymbol{\eta}) = \hat{\rho}(\xi)$ , meaning that  $\hat{\alpha}(\boldsymbol{\eta}) \equiv 1$ . A closer look on formula (4) reveals that

$$\nabla_{\mathbf{x}}\phi(\mathbf{x}) = [\mathbf{J}_K(1, \boldsymbol{\eta})]^{-T} \hat{\rho}'(\xi). \quad (7)$$

For affine elements  $K$  and  $\hat{\rho}(\xi) = \xi$ , the mapped function has constant gradient normal to  $L$ , so that  $\phi \in H^1(K)$  is an affine function vanishing at the collapsed vertex  $\mathbf{a}_1$ , and constant unitary values  $\phi|_L \equiv 1$  over the facet  $L$  opposite to  $\mathbf{a}_1$ .

### 3. SBFEM spaces in the context of Duffy's approximations

Our purpose in this section is to summarize the main aspects of SBFEM approximation spaces under the point of view of Duffy's approximations and to prove some of their orthogonality properties to a large range of  $H^1$ -conforming functions.

#### 3.1. $S$ -elements

The SBFEM adopts macro partitions  $\mathcal{T} = \{S\}$  of the computational domain  $\Omega \subset \mathbb{R}^d$  by subregions  $S$  verifying the starlike scaling requirement that any point on the boundary of  $S$  should be directly visible from a point  $\mathbf{O} \in S$ , called the scaling center. We restrict the study to convex polytopal  $S$ -elements (polygonal or polyhedral with flat facets  $L^e$ ). In the literature covering this method, the set  $\Gamma^S = \cup_e L^e$ ,  $e = 1, \dots, N^{\Gamma^S}$  is known as the scaled boundary element. A conformal sub-partition  $\mathcal{T}^S = \{K^e\}$  of  $S$  is formed by sectors  $K^e$  sharing the scaling center  $\mathbf{O}$  as one of their vertices,  $L^e$  being the facet of  $K^e$  opposite to the scaling center. As illustrated in Figure 4, the sectors  $K^e$  may have different geometry: triangular in 2D, pyramidal, or tetrahedral in 3D, the facets  $L^e$  being a line segment, a quadrilateral or a triangular element, respectively. Moreover, we notice that a three-dimensional  $S$ -element may also be partitioned by hybrid tetrahedral-pyramidal meshes, combining elements of different geometry, with scaled boundary  $\Gamma^S$  formed by triangular-quadrilateral facets. For simplicity, we shall restrict the analysis to partitions  $\mathcal{T}^S$  where all elements  $K^e$  have the same geometry.

This scaled geometry of  $S$  implies that the points  $\mathbf{x} \in S$  can be uniquely represented by a radial coordinate  $0 \leq \xi \leq 1$  and a surface coordinate  $\mathbf{x}_b$ . The radial coordinate (or scaling factor) points from the scaling center ( $\xi = 0$ ) to a point  $\mathbf{x}_b \in \Gamma^S$  (where  $\xi = 1$ ). The geometry of  $S$  may also be defined in each sector  $K^e \in \mathcal{T}^S$  by a transformation from the cartesian coordinates  $\mathbf{x} \in K^e$  to parametric Duffy's coordinates  $(\xi, \boldsymbol{\eta}) \in \hat{K} = [0, 1] \times \hat{L}$ . This correspondence defines a geometric mapping  $F_{K^e} : \hat{K} \rightarrow K^e$  in the class of Duffy's transformations described in the previous section, where  $K^e$  is interpreted as a collapsed quadrilateral, hexahedral or prismatic geometric element for which the facet  $F_{K^e}(0, \boldsymbol{\eta})$  is collapsed on top of its vertex  $\mathbf{x}_0$  in the scaling center  $\mathbf{O}$ . The points  $\mathbf{x}_b$  in the opposed facet  $L^e$  are expressed as  $F_{K^e}(1, \boldsymbol{\eta}) = F_{L^e}(\boldsymbol{\eta})$ ,  $\boldsymbol{\eta} \in \hat{L}$ . For hexahedral or prismatic reference elements  $\hat{K}$ , the lateral quadrilateral faces are collapsed on triangular faces to form a pyramid or a tetrahedron, respectively. These maps are illustrated in Figure 4.

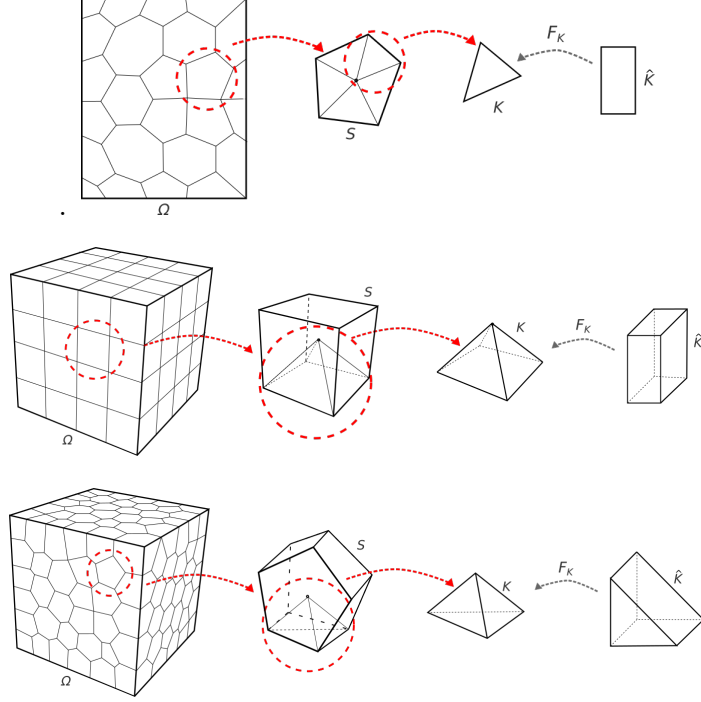


Figure 4: Illustration of macro partitions  $\mathcal{T} = \{S\}$ , with focus on a sector  $K \in \mathcal{T}^S$ , with corresponding Duffy's transformation, for triangular, pyramidal and tetrahedral  $K$ .

### 3.2. Duffy's spaces in $S$ -elements

There are two stages in the construction of approximations on polytopal elements  $S$ :

- 1) Definition of a trace space over the boundary  $\Gamma^S$ .
- 2) Extension of the traces to the interior of  $S$ .

The first stage is typical of FE contexts, but for specific scaled  $S$ -elements the extension to the interior can be performed in the radial direction.

#### Trace FE space over the scaled boundary $\Gamma^S$

Let  $\Lambda_k(\Gamma^S) = C(\Gamma^S) \cap \prod_{L^e \subset \Gamma^S} V_k(L^e)$  be a FE space defined over  $\Gamma^S$ . Recall that  $V_k(L^e) = \mathbb{F}_{L^e}(V_k(\hat{L}))$ , where  $V_k(\hat{L})$  is the polynomial space considered in  $\hat{L}$ . Let  $N_k^{l,e} = \mathbb{F}_{L^e}(\hat{N}_k^l)$  be shape functions for the local FE spaces  $V_k(L^e)$  over the facets  $L^e \subset \Gamma^S$  obtained backtracking polynomial shape functions  $\hat{N}_k^l$  for the reference polynomial space  $V_k(\hat{L})$ . Thus, if  $\alpha \in \Lambda_k(\Gamma^S)$  and  $\mathbf{x}_b = F_{L^e}(\boldsymbol{\eta}) \in L^e$ , then  $\alpha(\mathbf{x}_b) = \hat{\alpha}^e(\boldsymbol{\eta}) = \sum_l \alpha^{l,e} \hat{N}_k^l(\boldsymbol{\eta})$ . As usual, shape functions  $N_k^{n,S}(\mathbf{x})$  for  $\Lambda_k(\Gamma^S)$  (say, of cardinality  $\mathcal{N}^S$ ) can be obtained by the assembly of the local shape functions  $N_k^{l,e}$ , and the functions  $\alpha \in \Lambda_k(\Gamma^S)$  can globally be represented by linear combinations  $\alpha(\mathbf{x}_b) = \sum_{n=1}^{\mathcal{N}^S} \alpha^n N_k^{n,S}(\mathbf{x}_b)$ ,  $\mathbf{x}_b \in \Gamma^S$ . By collecting the shape functions and multiplying coefficient in  $\mathcal{N}^S$ -vectors  $\underline{N}^S = [N_k^{n,S}]$  and  $\underline{\alpha} = [\alpha^n]$ , we may use the alternative expression  $\alpha = \underline{N}^S \cdot \underline{\alpha}$ .

#### Radial extensions: Duffy's space over $S$

Given a trace function  $\alpha \in \Lambda_k(\Gamma^S)$ , take a radial function  $\hat{\rho}(\xi)$ ,  $0 \leq \xi \leq 1$ , to induce the definition of a function  $\phi(\mathbf{x})$  by radial extension to the interior of  $S$ . Inside each

sector  $K^e \in \mathcal{T}^S$  and over  $L^e$ , consider the parametrizations  $\mathbf{x} = F_{K^e}(\xi, \boldsymbol{\eta}) \in K^e$  and  $\mathbf{x}_b = F_{L^e}(\boldsymbol{\eta})$ . Recall the representation  $\alpha(\mathbf{x}_b) = \hat{\alpha}^e(\boldsymbol{\eta})$  to define the radial extension

$$\phi(\mathbf{x}) = \hat{\phi}^e(\xi, \boldsymbol{\eta}) := \hat{\rho}(\xi)\hat{\alpha}^e(\boldsymbol{\eta}).$$

Notice that the surface component  $\hat{\alpha}^e(\boldsymbol{\eta})$  varies over the partition  $\mathcal{T}^S$ , whilst the radial component  $\hat{\rho}(\xi)$  is the same in all sectors  $K^e$ .

Thus, we are in the following context of Duffy's approximation spaces

$$\mathcal{D}_k(S) = \left\{ \phi \in H^1(S); \exists \hat{\phi} \in \mathcal{D}_k(\hat{K}) \text{ such that } \phi|_{K^e} = \mathbb{F}_{K^e}(\hat{\phi}^e), \forall K^e \in \mathcal{T}^S \right\}, \quad (8)$$

where  $\hat{\mathcal{D}}_k(\hat{K})$  is a given reference Duffy's approximation space in the master element  $\hat{K}$  described in Section 2.2. For instance,  $\mathcal{D}_0(S)$  corresponds to the class of functions in association with  $\hat{\phi}^e(\xi, \boldsymbol{\eta}) = C\hat{\rho}(\xi), \forall K^e$ , obtained from constant trace functions  $\alpha \equiv C \in \Lambda_0(\Gamma^S)$ , where  $\Lambda_0(\Gamma^S)$  are the functions with constant value on  $\Gamma^S$ . It is clear that  $\mathcal{D}_0(S) \subset \mathcal{D}_k(S), \forall k \geq 0$ . Particularly, let us also consider the subspace  $\mathcal{D}_0^0(S) \subset \mathcal{D}_0(S)$  associated to radial functions  $\hat{\rho}(\xi)$  vanishing at  $\xi = 1$ .

So far,  $\mathcal{D}_k(S)$  is a functional space of infinite dimension, for discretization only happens for the surface component, living in a finite dimensional trace FE space  $\Lambda_k(\Gamma^S)$ , whilst the radial component can be chosen arbitrarily. The SBFEM spaces to be considered in Section 3.3 are examples of finite dimensional subspaces of  $\mathcal{D}_k(S)$ . Other finite dimensional subspaces  $\mathcal{D}_{k,m}(S) \subset \mathcal{D}_k(S)$  are also of interest: functions  $\phi$  having local components  $\phi|_{K^e} = \mathbb{F}_{K^e}(\hat{\phi}^e)$ , where  $\hat{\phi}^e(\xi, \boldsymbol{\eta}) = \hat{\rho}(\xi)\hat{\alpha}^e(\boldsymbol{\eta})$  with  $\hat{\rho} \in \mathbb{P}_m[0, 1]$  and  $\hat{\alpha}^e \in V_k(\hat{L})$ .

*Gradient inner product in  $\mathcal{D}_k(S)$*

Let a pair of functions  $\phi, \psi \in \mathcal{D}_k(S)$  with local components  $\phi|_{K^e} = \mathbb{F}_{K^e}(\hat{\phi}^e)$ , and  $\psi|_{K^e} = \mathbb{F}_{K^e}(\hat{\psi}^e)$ ,  $\hat{\phi}^e(\xi, \boldsymbol{\eta}) = \hat{\rho}(\xi)\hat{\alpha}^e(\boldsymbol{\eta})$ , and  $\hat{\psi}^e(\xi, \boldsymbol{\eta}) = \hat{\sigma}(\xi)\hat{\mu}^e(\boldsymbol{\eta})$  being associated with radial  $\hat{\rho}(\xi), \hat{\sigma}(\xi)$  and surface  $\hat{\alpha}^e(\boldsymbol{\eta}), \hat{\mu}^e(\boldsymbol{\eta})$  components. Recalling the trace representation  $\alpha(\mathbf{x}_b) = \hat{\alpha}^e(\boldsymbol{\eta}) = \sum_l \alpha_l^e \hat{N}_k^l(\boldsymbol{\eta})$  for  $\mathbf{x}_b \in L^e$ , then formula (5) becomes

$$\nabla_{\mathbf{x}}\phi(\mathbf{x}) = \sum_l \alpha^{l,e} \begin{bmatrix} \underline{B}_{1l}^e(\boldsymbol{\eta}) & \underline{B}_{2l}^e(\boldsymbol{\eta}) \end{bmatrix} \begin{bmatrix} \hat{\rho}'(\xi) \\ \frac{1}{\xi}\hat{\rho}(\xi) \end{bmatrix}, \quad \text{for } \mathbf{x} \in K^e,$$

both  $d \times 1$  matrices

$$\underline{B}_{1l}^e(\boldsymbol{\eta}) = \mathbf{J}_{K^e}(1, \boldsymbol{\eta})^{-T} \begin{bmatrix} \hat{N}_k^l(\boldsymbol{\eta}) \\ 0 \end{bmatrix}, \quad \underline{B}_{2l}^e(\boldsymbol{\eta}) = \mathbf{J}_{K^e}(1, \boldsymbol{\eta})^{-T} \begin{bmatrix} 0 \\ \nabla_{\boldsymbol{\eta}}\hat{N}_k^l(\boldsymbol{\eta}) \end{bmatrix}$$

depending on the geometry of the element at the boundary, and on the surface component, but being independent of the radial coordinate  $\xi$  (see [4] for the occurrence of these matrices in the formulation of SBFEM methods). Analogous formula holds for  $\psi$ :

$$\nabla_{\mathbf{x}}\psi(\mathbf{x}) = \sum_m \mu^{m,e} \begin{bmatrix} \underline{B}_{1m}^e(\boldsymbol{\eta}) & \underline{B}_{2m}^e(\boldsymbol{\eta}) \end{bmatrix} \begin{bmatrix} \hat{\sigma}'(\xi) \\ \frac{1}{\xi}\hat{\sigma}(\xi) \end{bmatrix}.$$

Thus, if  $\langle \phi, \psi \rangle_{\nabla, K^e} := \int_{K^e} \nabla_{\mathbf{x}}\phi(\mathbf{x}) \cdot \nabla_{\mathbf{x}}\psi(\mathbf{x}), dK^e$ , then

$$\begin{aligned} \langle \phi, \psi \rangle_{\nabla, K^e} &= \sum_{l,m} \mu^{m,e} \alpha^{l,e} \int_0^1 \int_{-1}^1 \begin{bmatrix} \underline{B}_{1l}^e & \underline{B}_{2l}^e \end{bmatrix} \begin{bmatrix} \hat{\rho}'(\xi) \\ \frac{1}{\xi}\hat{\rho}(\xi) \end{bmatrix} \cdot \begin{bmatrix} \underline{B}_{1m}^e & \underline{B}_{2m}^e \end{bmatrix} \begin{bmatrix} \hat{\sigma}'(\xi) \\ \frac{1}{\xi}\hat{\sigma}(\xi) \end{bmatrix} \xi^{d-1} |\mathbf{J}_{K^e}(1, \boldsymbol{\eta})| d\boldsymbol{\eta} d\xi \\ &= \sum_{l,m} \mu^{m,e} \alpha^{l,e} \int_0^1 \int_{-1}^1 \begin{bmatrix} \hat{\rho}'(\xi) & \frac{1}{\xi}\hat{\rho}(\xi) \end{bmatrix} \cdot \left( \begin{bmatrix} \underline{B}_{1l}^{eT} \\ \underline{B}_{2l}^{eT} \end{bmatrix} \begin{bmatrix} \underline{B}_{1m}^e & \underline{B}_{2m}^e \end{bmatrix} |\mathbf{J}_{K^e}(1, \boldsymbol{\eta})| \right) \begin{bmatrix} \hat{\sigma}'(\xi) \\ \frac{1}{\xi}\hat{\sigma}(\xi) \end{bmatrix} \xi^{d-1} d\boldsymbol{\eta} d\xi \\ &= \sum_{l,m} \mu^{m,e} \alpha^{l,e} \int_0^1 \begin{bmatrix} \hat{\rho}'(\xi) & \frac{1}{\xi}\hat{\rho}(\xi) \end{bmatrix} \underline{E}_{ml}^e \begin{bmatrix} \hat{\sigma}'(\xi) \\ \frac{1}{\xi}\hat{\sigma}(\xi) \end{bmatrix} \xi^{d-1} d\xi, \end{aligned} \quad (9)$$

where the entries in the matrix  $\underline{\underline{E}}_{ml}^e = \begin{bmatrix} E_{11,ml}^e & E_{12,ml}^e \\ E_{21,ml}^e & E_{22,ml}^e \end{bmatrix}$  are

$$\begin{aligned} E_{11,ml}^e &= \int_{-1}^1 \underline{B}_{1l}^{eT}(\boldsymbol{\eta}) \underline{B}_{1m}^e(\boldsymbol{\eta}) |\mathbf{J}_{K^e}(1, \boldsymbol{\eta})| \, d\boldsymbol{\eta}, & E_{12,lm}^e &= \int_{-1}^1 \underline{B}_{1l}^{eT}(\boldsymbol{\eta}) \underline{B}_{2,m}^e(\boldsymbol{\eta}) |\mathbf{J}_{K^e}(1, \boldsymbol{\eta})| \, d\boldsymbol{\eta}. \\ E_{21,ml}^e &= \int_{-1}^1 \underline{B}_{2l}^{eT}(\boldsymbol{\eta}) \underline{B}_{1m}^e(\boldsymbol{\eta}) |\mathbf{J}_{K^e}(1, \boldsymbol{\eta})| \, d\boldsymbol{\eta}, & E_{22,lm}^e &= \int_{-1}^1 \underline{B}_{2l}^{eT}(\boldsymbol{\eta}) \underline{B}_{2,m}^e(\boldsymbol{\eta}) |\mathbf{J}_{K^e}(1, \boldsymbol{\eta})| \, d\boldsymbol{\eta}. \end{aligned}$$

### 3.3. SBFEM spaces in $S$ -elements

There are two stages in the construction of local SBFEM approximation spaces in  $S$ -elements, that we shall denote by  $\mathbb{S}_k(S)$ : the restriction of a function in  $\mathbb{S}_k(S)$  over the scaled boundary  $\Gamma^S$  is set in the FE trace space  $\Lambda_k(\Gamma^S)$ , and in the radial direction, it is obtained analytically in terms of eigenvectors and eigenfunctions of an ODE system, known SBFEM equation. Our purpose is to highlight the main aspects of SBFEM spaces in the context of Duffy's approximations  $\mathcal{D}_k(S)$  for  $S$ -elements, and to show that a paramount for the derivation of the SBFEM equation is the enforcement of a gradient orthogonality constraint.

Precisely, having in mind that our goal is the solution of harmonic model problems, let us define the subspace

$$\mathbb{S}_k(S) = \left\{ \phi \in \mathcal{D}_k(S); \langle \phi, \psi \rangle_{\nabla, S} := \int_S \nabla_{\mathbf{x}} \phi(\mathbf{x}) \cdot \nabla_{\mathbf{x}} \psi(\mathbf{x}) \, dS = 0, \forall \psi \in \mathcal{D}_0^0(S), \psi(\mathbf{O}) = 0 \right\}. \quad (10)$$

This definition suggests that the functions  $\phi \in \mathbb{S}_k(S) \subset \mathcal{D}_k(S)$  have boundary values  $\phi|_{\Gamma^S} = \alpha \in \Lambda_k(\Gamma^S)$ , and they are “weak solutions” of the harmonic equation  $\Delta \Phi = 0$  in  $S$  with Dirichlet data  $\alpha$ . Thus, in some extent,  $\mathbb{S}_k(S)$  can be interpreted as “radial harmonic extensions” of the trace FE space  $\Lambda_k(\Gamma^S)$  to the interior of  $S$ .

Notice that  $\phi_0(\mathbf{x}) \equiv 1$  is clearly in  $\mathbb{S}_k(S)$ . The goal is to construct linearly independent shape functions  $\phi_i \in \mathbb{S}_k(S)$  such that

$$\mathbb{S}_k(S) = \text{span} \{ \phi_i \}.$$

It is known that the radial components and boundary values for the SBFEM shape functions  $\phi_i$  are determined by a particular family of exact eigenvalues and eigenfunctions solving an ODE system [4]. Next, we recover this representation of  $\phi_i$  using the current approach of Duffy's approximations constrained by the gradient orthogonality property expressed in (10).

Recall that, as a function in  $\mathcal{D}_k(S)$ , the shape function  $\phi_i \in \mathbb{S}_k(S)$  must be obtained as  $\phi_i|_{K^e} = \mathbb{F}_{K^e}(\hat{\phi}_i^e)$ , backtracking a function  $\hat{\phi}_i^e(\xi, \boldsymbol{\eta}) = \hat{\rho}_i(\xi) \hat{\alpha}_i^e(\boldsymbol{\eta}) \in \hat{\mathcal{D}}_k(\hat{K})$ . Moreover, we are assuming that the local surface components  $\hat{\alpha}_i^e(\boldsymbol{\eta})$  have expressions  $\hat{\alpha}_i^e(\boldsymbol{\eta}) = \sum_l \alpha_i^{l,e} \hat{N}_k^l(\boldsymbol{\eta})$ , as linear combinations of shape functions  $\hat{N}_k^l(\boldsymbol{\eta}) \in V_k(\hat{L})$ . Thus, it is necessary to characterize the radial functions  $\hat{\rho}_i(\xi)$  and the multiplying coefficients  $\alpha_i^{l,e}$  allowing the verification of the gradient orthogonality property stated in definition (10).

#### Derivation of the SBFEM equation

Let  $\psi(\mathbf{x}) \in \mathcal{D}_k(S)$  be a general function locally defined as  $\psi|_{K^e} = \mathbb{F}_{K^e}(\hat{\psi}^e)$ , where  $\hat{\psi}^e(\xi, \boldsymbol{\eta}) = \hat{\sigma}(\xi) \hat{\mu}^e(\boldsymbol{\eta}) \in \hat{\mathcal{D}}_k(\hat{K})$  and consider its gradient inner product

$$\langle \phi_i, \psi \rangle_{\nabla, S} = \int_S \nabla_{\mathbf{x}} \phi_i(\mathbf{x}) \cdot \nabla_{\mathbf{x}} \psi(\mathbf{x}) \, dS = \sum_e \langle \phi_i, \psi \rangle_{\nabla, K^e},$$

with a (searched) shape function  $\phi_i \in \mathbb{S}_k(S)$ , where the terms  $\langle \phi_i, \psi \rangle_{\nabla, K^e}$  are expressed as in (9). In fact, this formula can be rewritten as:

$$\begin{aligned} \langle \phi_i, \psi \rangle_{\nabla, K^e} = \sum_{m,l} \mu^{m,e} \alpha^{l,e} \int_0^1 & \left( \xi^{d-1} \hat{\rho}'_i(\xi) E_{11,ml}^e \hat{\sigma}'(\xi) + \xi^{d-2} \hat{\rho}'_i(\xi) E_{12,ml}^e \hat{\sigma}(\xi) \right. \\ & \left. + \xi^{d-2} \hat{\rho}_i(\xi) E_{21,ml}^e \hat{\sigma}'(\xi) + \xi^{d-3} \hat{\rho}_i(\xi) E_{22,ml}^e \hat{\sigma}(\xi) \right) d\xi. \end{aligned} \quad (11)$$

Let us denote by  $\underline{E}_{rs}$ ,  $r, s \in \{1, 2\}$ , the  $\mathcal{N}^S \times \mathcal{N}^S$  matrices obtained by assembling the matrices  $\underline{E}_{rs,ml}^e$ , element-by-element, according to the interelement connectivity. The process is similar to matrix assembly for FE discretizations of boundary problems in  $\mathbb{R}^{d-1}$ . Moreover, consider the vector functions  $\hat{\underline{\Psi}}_i(\xi) = \hat{\rho}_i(\xi) \underline{\alpha}_i$ , and  $\hat{\underline{\Psi}}(\xi) = \hat{\sigma}(\xi) \underline{\mu}$  collecting both radial and trace information of the shape functions  $\phi_i(\mathbf{x})$  and of test functions  $\psi(\mathbf{x})$ . Applying this notation, and summing up the contributions in (11), we obtain

$$\begin{aligned} \langle \phi_i, \psi \rangle_{\nabla, S} = \int_0^1 \hat{\underline{\Psi}}'(\xi) \cdot & \left[ \xi^{d-1} \underline{E}_{11} \hat{\underline{\Phi}}'_i(\xi) + \xi^{d-2} \underline{E}_{21} \hat{\underline{\Phi}}_i(\xi) \right] + \\ \hat{\underline{\Psi}}(\xi) \cdot & \left[ \xi^{d-2} \underline{E}_{12} \hat{\underline{\Phi}}'_i(\xi) + \xi^{d-3} \underline{E}_{22} \hat{\underline{\Phi}}_i(\xi) \right] d\xi. \end{aligned} \quad (12)$$

Consider  $\hat{\underline{Q}}_i(\xi) = \left[ \xi^{d-1} \underline{E}_{11} \hat{\underline{\Phi}}'_i(\xi) + \xi^{d-2} \underline{E}_{21} \hat{\underline{\Phi}}_i(\xi) \right]$ , and apply integration by parts to obtain

$$\int_0^1 \hat{\underline{\Psi}}'(\xi) \cdot \hat{\underline{Q}}_i(\xi) d\xi = \hat{\underline{\Psi}} \cdot \hat{\underline{Q}}_i \Big|_0^1 - \int_0^1 \hat{\underline{\Psi}}(\xi) \cdot \hat{\underline{Q}}'_i(\xi) d\xi. \quad (13)$$

For  $\hat{\underline{Q}}'_i(\xi) = \underline{E}_{11} \left( \xi^{d-1} \hat{\underline{\Phi}}''_i(\xi) + (d-1) \xi^{d-2} \hat{\underline{\Phi}}'_i(\xi) \right) + \underline{E}_{21} \left( \xi^{d-2} \hat{\underline{\Phi}}'_i(\xi) + (d-2) \xi^{d-3} \hat{\underline{\Phi}}_i(\xi) \right)$ , the inclusion of formula (13) in (12) gives

$$\begin{aligned} \langle \phi_i, \psi \rangle_{\nabla, S} = \hat{\underline{\Psi}} \cdot \hat{\underline{Q}}_i \Big|_0^1 - \int_0^1 \hat{\underline{\Psi}}(\xi) \cdot & \left[ \xi^{d-1} \underline{E}_{11} \hat{\underline{\Phi}}''_i(\xi) + \left[ (d-1) \underline{E}_{11} - \underline{E}_{12} + \underline{E}_{21} \right] \xi^{d-2} \hat{\underline{\Phi}}'_i(\xi) \right. \\ & \left. + \left[ (d-2) \underline{E}_{21} - \underline{E}_{22} \right] \xi^{d-3} \hat{\underline{\Phi}}_i(\xi) \right] d\xi. \end{aligned} \quad (14)$$

Recall that the purpose is to characterize the functions  $\phi_i(\mathbf{x}) \in \mathcal{D}_k(S)$  such that the orthogonality property  $M_i = 0$  holds for all functions  $\psi \in \mathcal{D}_0^0(S)$ , i.e., vanishing on  $\Gamma^S$ , but also vanishing on the scaling center. That is, for  $\hat{\sigma}(0) = \hat{\sigma}(1) = 0$  and consequently  $\hat{\underline{\Psi}}(0) = \hat{\underline{\Psi}}(1) = 0$ . These constraints on  $\psi$  cancel the boundary term in (14). On the other hand, the condition for vanishing the integral term in (14) for all  $\hat{\underline{\Psi}}(\xi)$  is equivalent to say that  $\hat{\underline{\Phi}}(\xi)$  must solve the following equation

$$\xi^{d-1} \underline{E}_{11} \hat{\underline{\Phi}}''_i(\xi) + \left[ (d-1) \underline{E}_{11} - \underline{E}_{12} + \underline{E}_{21} \right] \xi^{d-2} \hat{\underline{\Phi}}'_i(\xi) + \left[ (d-2) \underline{E}_{21} - \underline{E}_{22} \right] \xi^{d-3} \hat{\underline{\Phi}}_i(\xi) = 0. \quad (15)$$

Notice that this is the usual scaled boundary equation documented in [4] for the SBFEM shape functions. The resolution of (15) is well documented in the SBFEM literature, and it involves an auxiliary eigenvalue problem for an ODE system in terms of both  $\hat{\underline{\Phi}}_i(\xi)$  and  $\hat{\underline{Q}}_i(\xi)$ . For self completeness, the methodology is briefly described in Appendix A.

In summary, the resulting solutions  $\hat{\underline{\Phi}}_i = \hat{\rho}_i(\xi) \underline{\alpha}_i$  have the form  $\hat{\rho}_i(\xi) = \xi^{\lambda_i}$ , and  $\underline{\alpha}_i = \underline{A}_i$ , where  $\lambda_i$  and  $\underline{A}_i$  refer to positive real parts of the eigenvalues and the associated eigenfunctions for the ODE system equivalent to the SBFEM equation (15). This

information is required for the construction of the SBFEM basis functions  $\phi_i$ , giving the radial components  $\hat{\rho}_i(\xi)$  and the trace surface components  $\alpha_i \in \Lambda_k(\Gamma^S)$  recovered from the coefficient vectors  $\underline{\alpha}_i$ . Thus, the corresponding expressions are

$$\phi_i(\mathbf{x}) = \hat{\phi}_i^e(\xi, \boldsymbol{\eta}) = \xi^{\lambda_i} \sum_l \underline{A}_i^{l,e} \hat{N}_k^l(\boldsymbol{\eta}), \text{ for } \mathbf{x} = F_{K^e}(\xi, \boldsymbol{\eta}) \in K^e. \quad (16)$$

Analogously, associated to  $\hat{Q}_i(\xi)$  are the flux functions

$$q_i(\mathbf{x}) = \hat{q}_i^e(\xi, \boldsymbol{\eta}) = \xi^{\lambda_i} \sum_l \underline{Q}_i^{l,e} \hat{N}_k^l(\boldsymbol{\eta}), \text{ for } \mathbf{x} = F_{K^e}(\xi, \boldsymbol{\eta}) \in K^e. \quad (17)$$

#### 3.4. Orthogonality properties of the SBFEM spaces

In this section, we highlight two kinds of gradient orthogonality properties held by the SBFEM approximation spaces.

##### *Intrinsic gradient orthogonality property for $\mathbb{S}_k(S)$*

The usual procedure for the construction of SBFEM shape functions is the determination of analytic eigenfunctions for the SBFEM equation (15). We have shown in the previous section that there is another characterization of these shape functions that are not well recognized. Namely, implicit in the condition for a function  $\phi \in \mathcal{D}_k(S)$  to solve the SBFEM equation (15) is the gradient orthogonality property, enforced from the start, in the definition of the subspaces  $\mathbb{S}_k(S)$  in (10). Precisely, a function  $\phi \in \mathbb{S}_k(S) \subset \mathcal{D}_k(S)$  if the gradient orthogonality constraint

$$\langle \phi, \psi \rangle_{\nabla, S} = \int_S \nabla_{\mathbf{x}} \phi(\mathbf{x}) \cdot \nabla_{\mathbf{x}} \psi(\mathbf{x}) dS = 0 \quad (18)$$

holds for all  $\psi \in \mathcal{D}_0^0(S)$ , with  $\psi(\mathbf{O}) = 0$ . In such case, then  $\phi$  solves equation (15).

##### *Extended gradient orthogonality property for $\mathbb{S}_k(S)$*

Let  $\mathcal{H}(S)$  denotes the space of harmonic functions in  $S$ . Then, it is clear that  $\langle \phi, \psi \rangle_{\nabla, S} = 0$  for all  $\phi \in \mathcal{H}(S)$  and  $\psi \in H_0^1(S)$ , giving the well-known decomposition

$$H^1(S) = \mathcal{H}(S) \overset{\nabla}{\oplus} H_0^1(S), \quad (19)$$

where the symbol  $\overset{\nabla}{\oplus}$  denotes the orthogonality relation with respect to the gradient inner product  $\langle \cdot, \cdot \rangle_{\nabla, S}$ . Our purpose is to show a similar relation for Duffy's spaces  $\mathcal{D}_k(S) \subset H^1(S)$ ,  $\mathbb{S}_k(S)$  playing the role of the harmonic functions. For that, we need to extend the gradient orthogonality property (18) to functions  $\psi \in \mathcal{D}_0(S)$ .

**Proposition 3.1.** *The orthogonality property*

$$\langle \phi, \psi \rangle_{\nabla, S} = 0, \quad \forall \phi \in \mathbb{S}_k(S) \text{ and } \psi \in \mathcal{D}_0(S) \quad (20)$$

is valid. Thus,

$$\mathcal{D}_k(S) = \mathbb{S}_k(S) \overset{\nabla}{\oplus} \mathcal{D}_0(S) \quad (21)$$

holds as a mimetic version of (19).

*Proof.* A crucial step in the derivation of the SBFEM equation (15) is the formula for the gradient inner product  $\langle \phi, \psi \rangle_{\nabla, S}$  given in (14), where two terms enter into play: a boundary term and an integral term. The constraints  $\psi \in \mathcal{D}_0^0(S)$  and  $\psi(\mathbf{O}) = 0$  make the boundary term to be zero, and (15) derives from the assumption (18).

Now let us relax the constraints  $\psi \in \mathcal{D}_0^0(S)$  and  $\psi(\mathbf{O}) = 0$ . Instead, take  $\psi$  in a broader space  $\mathcal{D}_0(S)$ . Clearly, the property  $\langle \phi, \psi \rangle_{\nabla, S} = 0$  holds for  $\phi = \phi_0 \equiv 1$ . Thus, it is sufficient to verify it for all shape functions  $\phi = \phi_i$  associated with eigenvalues  $\lambda_i \neq 0$ .

Notice that the desired orthogonality property (20) is valid for  $\psi \in \mathcal{D}_0(S)$ , with  $\hat{\psi}^e(\xi, \boldsymbol{\eta}) = C\hat{\sigma}(\xi)$  in the sectors  $K^e$ , if and only if it holds for functions  $\varphi = \psi - C\hat{\sigma}(1) \in \mathcal{D}_0^0(S)$ , i.e., for the cases where  $\hat{\varphi}(\xi) = C(\hat{\sigma}(\xi) - \hat{\sigma}(1))$ , with  $\hat{\varphi}(1) = 0$ . For them, we apply equation (15), valid for all shape functions  $\phi_i \in \mathbb{S}_k(S)$ , to reduce the equation (14) to

$$\langle \phi_i, \varphi \rangle_{\nabla, S} = \hat{\varphi}(1) \sum_n \hat{Q}_{in}(1) - \hat{\varphi}(0) \sum_n \hat{Q}_{in}(0).$$

Thus, since  $\hat{\varphi}(1) = 0$  and  $\hat{Q}_{in}(0) = 0$ , we obtain the orthogonality property (20).  $\square$

#### 4. Interpolants

When a Galerkin method is used to approximate a boundary value problem, one of the most important choices is the family of approximation spaces. For elliptic problems the achievable error of approximation is equal to the error obtained by approximating the solution of the partial differential equation directly from the trial space. The accuracy is accessed *a priori* by bounds computed in terms of interpolant errors using the approximation space. In the context of piecewise defined approximations over subregions (elements) of the computational domain, as is the case of FE methods, the interpolants usually show the following characteristics:

- **Locality:** in each subregion, a polynomial trace interpolant over the boundary is extended to the interior (a process also called lifting).
- **Global conformity:** it follows directly from the hypothesis that the trace interpolants depend exclusively on the function restriction over subregion boundaries.
- **Optimality:** optimal interpolation error estimates are achieved with respect to the discretization parameters: mesh width and polynomial order.

In this direction, the plan is to construct interpolants in SBFEM trial spaces, and to explore them to evaluate the potential of SBFEM approximations. Firstly, let us introduce some new notation and auxiliary results already known in other contexts.

Consider a family of conformal polytopal partitions  $\mathcal{T}^h = \{S\}$  of  $\Omega$  by  $S$ -elements, as described in Section 3.1. Define the mesh skeleton  $\Gamma^h = \cup_{L \in \mathcal{E}^h} L$  by the assembly of all facets (edges of faces) in  $\mathcal{E}^h = \{L \subset \Gamma^{h,S}, S \in \mathcal{T}^h\}$ . The parameter  $h$  refers to the characteristic size of the facets in  $\Gamma^h$ . Moreover, define the conglomerate partitions  $\mathcal{P}^h = \cup_{S \in \mathcal{T}^h} \mathcal{T}^{h,S}$  of  $\Omega$ . Recall that the elements  $K \in \mathcal{T}^{h,S}$  may be affine triangles, pyramids, or tetrahedra inheriting the conformal property from  $\mathcal{T}^h$ . In principle, shape regularity of  $\mathcal{P}^h$  is not a granted property.

Based on the partitions  $\Gamma^h$ ,  $\mathcal{T}^h$  or  $\mathcal{P}^h$ , we consider the following approximation spaces.

- **FE trace spaces:**  $\Lambda_k(\Gamma^h) = C^0(\Gamma^h) \cap \prod_{L \in \mathcal{E}^h} V_k(L)$ , piecewise polynomial spaces, where  $V_k(L) = \mathbb{P}_k(L)$ , for 1D edges and triangular facets  $L$ , and  $V_k(L) = \mathbb{Q}_{k,k}(L)$ , for quadrilateral facets  $L$ .

- Duffy's spaces  $\mathcal{D}_k^h \subset H^1(\Omega)$ : given the local Duffy's spaces  $\mathcal{D}_k^h(S), S \in \mathcal{T}^h$  defined in Section 3.2, set

$$\begin{aligned}\mathcal{D}_k^h &= \{w \in H^1(\Omega); w|_S \in \mathcal{D}_k^h(S), S \in \mathcal{T}^h\}, \\ \mathcal{D}_0^{0,h} &= \{w \in H^1(\Omega); w|_S \in \mathcal{D}_0^0(S), S \in \mathcal{T}^h\}.\end{aligned}$$

Notice that  $\mathcal{D}_0^{0,h} \subset \mathcal{D}_k^h, \forall k \geq 0$ .

- SBFEM spaces  $\mathbb{S}_k^h \subset H^1(\Omega)$ : given local SBFEM spaces  $\mathbb{S}_k^h(S) \subset \mathcal{D}_k^h(S), S \in \mathcal{T}^h$ , described in Section 3.3, define

$$\mathbb{S}_k^h = \{w \in H^1(\Omega); w|_S \in \mathbb{S}_k^h(S), S \in \mathcal{T}^h\},$$

and set  $\mathbb{S}_{k,0}^h = \mathbb{S}_k^h \cap H_0^1(\Omega)$ .

- FE spaces  $\mathcal{V}_k^{h,FE} \subset H^1(\Omega)$ : Consider the following FE spaces based on the conglomerated meshes  $\mathcal{P}^h$ .

1. Triangular (2D) and tetrahedral (3D) meshes  $\mathcal{P}^h$ :  $\mathcal{V}_k^{h,FE} := \mathbb{P}_k(\mathcal{P}^h) \cap H^1(\Omega)$ , where  $\mathbb{P}_k(\mathcal{P}^h)$  stands for functions piecewise defined by polynomials in  $\mathbb{P}_k(K), K \in \mathcal{P}^h$ , of degree not greater than  $k$ .
2. Pyramidal (3D) meshes  $\mathcal{P}^h$ : let us consider  $\mathcal{V}_k^{h,FE} := \mathcal{U}^{(0),k}(\mathcal{T}^h) \cap H^1(\Omega)$ , piecewise defined by a class of rational polynomials  $\mathcal{U}^{(0),k}(K)$ , for  $K \in \mathcal{P}^h$  [27]. Traces of functions in  $\mathcal{U}^{(0),k}(K)$  are in  $\mathbb{P}_k(L)$  for triangular faces, and in  $\mathbb{Q}_{k,k}(L)$  if  $L$  is quadrilateral. Moreover,  $\mathbb{P}_k(K) \subset \mathcal{U}^{(0),k}(K)$ .

**Proposition 4.1.** (i) For  $w \in \mathcal{V}_k^{h,FE}$ ,  $w|_{\Gamma^h} \in \Lambda_k(\Gamma^h)$ . (ii)  $\mathbb{P}_k(\mathcal{P}^h) \subset \mathcal{V}_k^{h,FE} \subset \mathcal{D}_k^h$ .

*Proof.* The trace property (i) and the polynomial inclusion in (ii) are already known. To proof the second embedding property in (ii), let us start by considering three particular collapsed triangular, pyramidal and tetrahedral reference elements.

- *A triangular reference element  $K$* : Let  $K$  be the reference triangle, with collapsed vertex  $\mathbf{a}_0 = (0, 0)$ , and the opposed edge  $L = [\mathbf{a}_1, \mathbf{a}_2]$ , where  $\mathbf{a}_1 = (1, 0)$  and  $\mathbf{a}_2 = (1, 1)$ . Taking the mapping  $F_L : \hat{L} \rightarrow L$ , defined as  $F_L(\boldsymbol{\eta}) = \left(\frac{1+\boldsymbol{\eta}}{2}, \frac{1-\boldsymbol{\eta}}{2}\right)$ , the Duffy's transformation from  $\hat{K}$  over  $K$  becomes  $x = \frac{\xi}{2}(1 + \boldsymbol{\eta})$ ,  $y = \frac{\xi}{2}(1 - \boldsymbol{\eta})$ , whose inversion is  $\xi = x + y$ ,  $\boldsymbol{\eta} = \frac{x-y}{x+y}$ . Let  $\psi \in \mathcal{D}_k(K)$  be the pullback of functions  $\mathbb{F}_K(\hat{\psi}) \in \mathcal{D}_k(\hat{K})$ , where  $\hat{\psi}(\xi, \boldsymbol{\eta}) = \xi_k \hat{\alpha}(\boldsymbol{\eta})$ , so that  $\psi(x, y) = (x + y)_k \hat{\alpha}\left(\frac{x-y}{x+y}\right)$ . Thus, by varying  $\hat{\alpha} \in \mathbb{P}_k(\hat{L})$ , we conclude that all functions  $\psi(x, y) \in \mathbb{P}_k(K)$  can be recovered in  $\mathcal{D}_k(K)$ .
- *A pyramidal reference element*: Suppose  $K$  is a pyramid with vertex  $\mathbf{a}_0 = (0, 0, 1)$ , and opposed face  $L = [\mathbf{a}_1, \mathbf{a}_2, \mathbf{a}_3, \mathbf{a}_4]$ , with vertices  $\mathbf{a}_1 = (0, 0, 0)$ ,  $\mathbf{a}_2 = (1, 0, 0)$ ,  $\mathbf{a}_3 = (1, 1, 0)$ , and  $\mathbf{a}_4 = (0, 1, 0)$ . The FE space  $\mathcal{U}^{(0),k}(K) \subset H^1(K)$  proposed in [27] is the first space of an exact sequence  $\mathcal{U}^{(s),k}(K)$  verifying the De Rham commuting property. Their definition considers the the geometric transformation  $S_\infty : K_\infty \rightarrow K$  of the "infinite pyramid"  $K_\infty = \{(x, y, z) \in \mathbb{R}^3; x, y, z \geq 0, x \leq 1, y \leq 1\} \cup \{\infty\}$ , given by  $S_\infty(x, y, z) = \left(\frac{x}{1+z}, \frac{y}{1+z}, \frac{z}{1+z}\right)$ ,  $S_\infty(\infty) = \mathbf{a}_0$ . The functions  $w \in \mathcal{U}^{(0),k}(K)$  are obtained by the pullback  $\mathbb{S}_\infty(u)$  of functions  $u$  in a properly chosen subspace of the rational functions  $\mathcal{Q}_k^{k,k,k}(\hat{K}_\infty) = \left\{\frac{q}{1+z}; q \in \mathbb{Q}_{k,k,k}(K_\infty)\right\}$ . Our goal is to show

that  $\mathcal{U}^{(0),k}(K)$  can also be interpreted in the context of the Duffy's space  $\mathcal{D}_k(K)$ . For that, consider the hexahedron  $H = [0, 1] \times [0, 1] \times [0, 1]$ , with the coordinate system  $(\mu_1, \mu_2, \xi)$ , with  $(\mu_1, \mu_2) \in [0, 1] \times [0, 1]$  and  $0 \leq \xi \leq 1$ . Observe that the geometric transformation  $F_\infty : H \rightarrow K_\infty$ ,  $F_\infty(\mu_1, \mu_2, \xi) = (\mu_1, \mu_2, \frac{\xi}{1-\xi})$  collapses the face  $\xi = 1$  in  $H$  onto  $\infty$ . Moreover,  $Q_k^{k,k,k}(\hat{K}_\infty) = \mathbb{F}_\infty(\mathbb{Q}_{k,k,k}(H))$ . Consequently,

$$\mathcal{U}^{(0),k}(K) \subset \mathbb{S}_\infty(Q_k^{k,k,k}(\hat{K}_\infty)) = \mathbb{S}_\infty(\mathbb{F}_\infty(\mathbb{Q}_{k,k,k}(H))). \quad (22)$$

On the other hand, the transformation  $F_K : H \rightarrow K$ , defined by the composition  $\mathbf{x} = F_K(\eta_1, \eta_2, \xi) = S_\infty(F_\infty(\eta_1, \eta_2, \xi))$  results to be a Duffy's transformation collapsing the face  $\xi = 1$  in  $H$  on top of the vertex  $\mathbf{a}_0 \in K$ . Consequently,  $\mathbb{F}_K(\mathbb{Q}_{k,k,k}(H)) \subset \mathcal{D}_k(K)$ . Thus, using (22), we obtain  $\mathcal{U}^{(0),k}(K) \subset \mathcal{D}_k(K)$ .

- *A tetrahedral reference element:* Suppose  $K$  is the reference tetrahedron with collapsed vertex  $\mathbf{a}_0 = (0, 0, 0)$ , and opposed quadrilateral face  $L = [\mathbf{a}_1, \mathbf{a}_2, \mathbf{a}_3]$ , with  $\mathbf{a}_1 = (1, 0, 1)$ ,  $\mathbf{a}_2 = (1, 0, 0)$  and  $\mathbf{a}_3 = (1, 1, 0)$ . Notice that  $L$  can be mapped by  $\mathbf{x} = F_L(\boldsymbol{\eta})$ , where  $x = 1 - \eta_1 - \eta_2$ ,  $y = \eta_1$ , and  $z = \eta_2$ . Then, the Duffy's transformation is  $F_K(\xi, \boldsymbol{\eta}) = \xi F_L(\boldsymbol{\eta})$ , whose inverse is  $\xi = x + y + z$ ,  $\eta_1 = \frac{y}{x+y+z}$ ,  $\eta_2 = \frac{z}{x+y+z}$ . Let  $\psi = \mathbb{F}_K(\hat{\psi}) \in \mathcal{D}_k(K)$ , with  $\hat{\psi}(\xi, \boldsymbol{\eta}) = \xi_k \hat{\alpha}(\boldsymbol{\eta})$ , and  $\hat{\alpha} \in \mathbb{P}_k(\hat{L})$ . Thus, the functions  $\psi(x, y, z) = (x + y + z)_k \hat{\alpha}(\frac{y}{x+y+z}, \frac{z}{x+y+z})$  recover all functions in  $\mathbb{P}_k(K)$ .

Now consider a general element  $K^e \in \mathcal{P}^h$ , with collapsed vertex  $\mathbf{O}$ , and opposed face  $L^e$  with vertices  $\mathbf{a}_l^e$ . Notice that  $K^e$  can be seen as a geometric affine transformation of one of the reference elements  $K$  described above, i.e.,  $K^e = T^e(K)$ , such that  $\mathbf{O} = T^e(\mathbf{a}_0)$ ,  $\mathbf{a}_l^e = T^e(\mathbf{a}_l)$ , and thus  $L^e = T^e(L)$ . Since the polynomials  $\mathbb{P}_k(K)$ , for triangles and tetrahedra, and rational polynomials  $\mathbb{S}_k(K)$ , for pyramids, are preserved by affine transformations, then we conclude that  $\mathcal{V}_k^{h,FE} \subset \mathcal{D}_k^h$ .  $\square$

#### 4.1. FE interpolants

Interpolant operators  $\mathcal{F}_k^{h,FE} : H^s(\Omega) \rightarrow \mathcal{V}_k^{h,FE}$  have been designed as useful tools for functions in general Sobolev spaces  $H^s(\Omega)$ ,  $s \geq 1$ . As already mentioned, they are constructed by first defining a piecewise polynomial trace interpolant over the facets  $L \subset \partial K$  of each element  $K \in \mathcal{P}^h$ , and then by extending this trace interpolant to the interior of  $K$ . Let us recall some examples and error estimates already available in the literature. For them, we assume the affine conglomerate triangular, pyramidal or tetrahedral partitions  $\mathcal{P}^h$  are regular (e.g. quasi-uniform and shape regular, with parameters independent of  $h$ ). Under these circumstances, the following estimates hold.

- There are interpolants  $\mathcal{F}_k^{h,FE} w$  over FE spaces  $\mathcal{V}_k^{h,FE} = \mathbb{P}_k(\mathcal{P}^h) \cap H^1(\Omega)$  defined in [28] for triangles and in [29] for tetrahedra. Suppose  $w \in H^s(\Omega)$ ,  $s > \frac{3}{2}$  in 2D, and  $s > 2$  in 3D, then the estimate

$$|w - \mathcal{F}_k^{h,FE} w|_{H^1(\Omega)} \lesssim \frac{h^{\mu-1}}{k^{d-2}} \|w\|_{H^s(\Omega)}$$

holds for  $\mu = \min(k+1, s)$ , where the leading constant on the right side is independent of  $w$ ,  $h$ , and  $k$  (but depends on  $s$  and regularity parameters of  $\mathcal{P}^h$ ).

- There are also the projection-based interpolants, proposed by L. Demkowicz and coworkers, as expounded in [30, 31]. They admit a general form, without requiring

any specific geometric aspect, and have the flexibility to treat general local spaces, not necessarily polynomials. Note that such constructions may require additional regularity assumptions beyond the minimal  $H^1$ -conformity. Indeed, the trace interpolants may require interpolation at element vertices, requiring the regularity  $H^{1+s}$  with  $s > 1/2$  in 3D FE settings. For FE spaces  $\mathcal{V}_k^{h,FE} = \mathbb{P}_k(\mathcal{P}^h) \cap H^1(\Omega)$  based on tetrahedra, the error estimates stated in [31, Theorem 2.2] for projection based-interpolants  $\mathcal{F}_k^{h,FE} w$  have the non-optimal form

$$|w - \mathcal{F}_k^{h,FE} w|_{H^1(\Omega)} \lesssim (\ln k)^2 \left(\frac{h}{k}\right)^{d-2} |w|_{H^s}, \quad s > 3/2. \quad (23)$$

The suboptimal logarithmic factor appearing in (23) can be dropped in the  $k$ -version under the more stringent regularity assumption  $s \geq 2$  [32, Corollary 2.12].

- For pyramidal partitions  $\mathcal{P}^h$ , projection-based interpolants  $\mathcal{F}_k^{h,FE} w$  over the FE spaces  $\mathcal{U}^{(0),k}(\mathcal{T}^h)$  are defined in [27]. However, to the best of our knowledge, error estimates are still missing for them, but optimal  $h$ -convergence rates have been observed in numerical experiments presented in [33].

#### 4.2. SBFEM interpolant

As for the cases of FE spaces, we construct interpolant operators  $\Pi_k^h : H^s(\Omega) \rightarrow \mathbb{S}_k^h$ , for sufficiently smooth functions  $w \in H^s(\Omega)$ , following three steps: a trace interpolant  $\mathcal{I}_k^h : H^s(\Gamma^h) \rightarrow \Lambda_k(\Gamma^h)$ , local projections  $\Pi_k^{h,S} : H^s(S) \rightarrow \mathbb{S}_k(S)$  extending trace functions to the interior of the element, and assembly of local interpolants.

1. Trace interpolant  $\mathcal{I}_k^h : H^s(\Omega) \rightarrow \Lambda_k(\Gamma^h)$  - it is piecewise defined on the facets  $L \in \mathcal{E}^h$ , following any of the interpolation strategies used so far for the FE spaces  $\mathcal{V}_k^{h,FE}$ .
2. Local projections  $\Pi_k^{h,S} : H^{k+1}(S) \rightarrow \mathbb{S}_k(S)$ :  $\Pi_k^{h,S} w \in \mathcal{D}_k^{h,S}$  solves the problem

$$\langle \Pi_k^{h,S} w, v \rangle_{\nabla, S} = 0 \quad \forall v \in \mathcal{D}_0^0(S), \quad (24)$$

$$\Pi_k^{h,S} w|_{\Gamma^S} = \mathcal{I}_k^h w|_{\Gamma^S}. \quad (25)$$

Notice that equation (24) ensures that  $\Pi_k^{h,S} w \in \mathbb{S}_k(S)$  and the relation (25) enforces the trace constraint matching  $\Pi_k^{h,S} w$  to the trace interpolant of  $w$ . It is clear from these equations the interpretation of  $\Pi_k^{h,S}$  as "radial harmonic extension" of the trace interpolant  $\mathcal{I}_k^h w$  to the interior of  $S$ . Let  $\underline{\omega}^S$  be the coefficients in the expansion  $\mathcal{I}_k^h w(\mathbf{x}_b) = \sum_{n=1}^{\mathcal{N}^S} \omega^{n,S} N_k^{n,S}(\mathbf{x}_b)$ ,  $\mathbf{x}_b \in \Gamma^S$ . We seek for coefficients  $\underline{c} = [c_i]$  such that  $\Pi_k^{h,S} w = \sum_i c_i \phi_i^S \in \mathbb{S}_k^h(S)$ . According to the definition of the local spaces  $\mathbb{S}_k^h(S)$ , the solution is  $\underline{c} = \underline{\omega}^S \underline{A}^{-1}$ , where  $\underline{A} = \underline{A}^S$  is the eigenvector matrix associated to the traces of the SBFEM shape-functions  $\phi_i^S$  over  $\Gamma^S$ .

3. Assembly - Define  $\Pi_k^h w$  by assembling the local contributions  $\Pi_k^h w|_S = \Pi_k^{h,S} w$ . It is clear that  $\Pi_k^{h,S} w|_L = \Pi_k^{h,S} w|_L$  over an interface  $L = S \cap S'$  shared by two S-elements. Thus, the conformity property  $\Pi_k^h w \in H^1(\Omega)$  holds.

*Remarks*

- (1) In the same manner as FE interpolants  $\mathcal{F}_k^{h,FE} w$ , the SBFEM interpolant  $\Pi_k^h$  satisfies the two fundamental properties: locality and global conformity. However, they differ on the way the trace interpolant is extended to the interior of the  $S$ -elements by their local projections. Recall that the "radial harmonic extension" adopted in the SBFEM context is possible due to the particular scaled geometry of the  $S$ -elements. Moreover, when the SBFEM interpolant shares the trace interpolant of  $\mathcal{F}_k^{h,FE} w$ , then it is clear that

$$\Pi_k^h w = \Pi_k^h \mathcal{F}_k^{h,FE} w. \quad (26)$$

- (2) Since  $\mathcal{I}_k^h w = w|_{\Gamma^h}$  for functions  $w \in \mathcal{D}_k^h$ , the trace constraint (25) means that  $w - \Pi_k^h w \in \mathcal{D}_0^{0,h}$  for all functions  $w$  in the Duffy's space  $\mathcal{D}_k^h$ . Consequently, Proposition 3.1 implies the orthogonality property

$$\langle w - \Pi_k^h w, v \rangle_{\nabla} = \sum_{S \in \mathcal{T}^h} \langle w - \Pi_k^{h,S} w, v \rangle_{\nabla, S} = 0, \quad \forall w \in \mathcal{D}_k^h, \quad \forall v \in \mathbb{S}_k^h. \quad (27)$$

*4.3. Comments on the SBFEM interpolation errors*

Unlike general purpose FE techniques, SBFEM approximations are constructed to be applied for a specific type of problem. Thus, for the model Laplace problem under consideration, there is no interest in accessing the accuracy of SBFEM interpolants  $\Pi_k^h w$  when applied to other than for harmonic functions  $w \in \mathcal{H}(\Omega)$ . For them, the sources of SBFEM interpolation errors are two-fold:

- (i) the polynomial discretization of traces  $w|_{\Gamma^h} \approx \mathcal{I}_k^h w \in \Lambda_k^h$ .
- (ii) the deviation of  $\Pi_k^{h,S} w \in \mathbb{S}_k^h$  of being an harmonic function.

In this direction, let us consider the subspaces

$$\mathcal{V}_k^{h,\Delta} = \{w \in \mathcal{H}(\Omega); w|_{\Gamma^h} \in \Lambda_k(\Gamma^h)\},$$

where only trace discretization takes place. Denoted by harmonic virtual spaces, they have been used in the context of the operator adapted virtual FE method proposed in [19], and designed to solve two-dimensional harmonic problems. The term "virtual" emphasizes that functions in  $\mathcal{V}_k^{h,\Delta}$  are not known explicitly in the interior of each subregion  $S \in \mathcal{T}^h$ .

The finite-dimensional spaces  $\mathcal{V}_k^{h,\Delta}$  have close similarities with the SBFEM spaces  $\mathbb{S}_k^h$ . In both cases, the trace functions are in  $\Lambda_k(\Gamma^h)$ , which are extended to the interior of the  $S$ -elements by solving local Dirichlet Laplace problems: whilst the functions in the local spaces  $V_k^\Delta(S) = \mathcal{V}_k^{h,\Delta}|_S$  are strongly harmonic in  $S$ , the ones in  $\mathbb{S}_k(S)$  are harmonic in a weaker sense. However, unlike for the harmonic subspaces  $V_k^\Delta(S)$ , it is possible to explore the radial Duffy's structure of  $\mathbb{S}_k^h(S)$  to explicitly compute shape functions for them, as described in the previous section.

Let us consider the harmonic virtual interpolant  $\mathcal{F}_k^{h,\Delta} : H^s(\Omega) \rightarrow \mathcal{V}_k^{h,\Delta}$  by solving the local Laplace problems

$$\langle \mathcal{F}_k^{h,\Delta} w, v \rangle_{\nabla, S} = 0 \quad \forall v \in H_0^1(S), \quad (28)$$

$$\mathcal{F}_k^{h,\Delta} w|_{\Gamma^S} = \mathcal{I}_k^h w|_{\Gamma^S}, \quad (29)$$

where the trace interpolant  $\mathcal{I}_k^h w$  is the one adopted in  $\Pi_k^h w$ . Note that this is an analytic recovery problem for it is not directly accessible for computation, whilst the SBFEM interpolant  $\Pi_k^h w$  is a computable recovery problem.

For an harmonic function  $u \in \mathcal{H}(\Omega)$ , let us consider the decomposition

$$u - \Pi_k^h u = (u - \mathcal{F}_k^{h,\Delta} u) + (\mathcal{F}_k^{h,\Delta} u - \Pi_k^h u) = (i) + (ii). \quad (30)$$

The first term  $(i) = u - \mathcal{F}_k^{h,\Delta} u$  compares two harmonic functions differing on the skeleton  $\Gamma^h$  by the trace interpolation error  $u - \mathcal{I}_k^h u$ , meaning that only the interface errors require to be estimated. In fact, the application of Neumann trace inequality ([34, Theorem A.33]) in each  $S$ -element  $S \in \mathcal{T}^h$  gives

$$|u - \mathcal{F}_k^{h,\Delta} u|_{H^1(S)} \lesssim \|u - \mathcal{I}_k^h u\|_{H^{\frac{1}{2}}(\partial S)}. \quad (31)$$

We refer to [19, Lemma 4.4, Lemma 4.5] for estimates of (31) in the particular Gauss-Lobatto trace interpolation case, and under some specific graded polygonal mesh circumstances. On the other hand, since

$$\Pi_k^h u = \Pi_k^h \mathcal{F}_k^{h,FE} u, \quad (32)$$

the second term becomes  $(ii) = \mathcal{F}_k^{h,\Delta} u - \Pi_k^h u = \mathcal{F}_k^{h,\Delta} u - \Pi_k^h \mathcal{F}_k^{h,\Delta} u$ , representing the SBFEM interpolation error for the harmonic virtual function  $\mathcal{F}_k^{h,\Delta} u \in \mathcal{V}_k^{h,\Delta}$ . Consequently, according to (24) and (28), we obtain

$$\langle \mathcal{F}_k^{h,\Delta} u - \Pi_k^h \mathcal{F}_k^{h,\Delta} u, v \rangle_{\nabla} = \sum_{S \in \mathcal{T}^h} \langle \mathcal{F}_k^{h,\Delta} u - \Pi_k^h \mathcal{F}_k^{h,\Delta} u, v \rangle_{\nabla, S} = 0, \quad \forall v \in \mathcal{D}_0^{0,h}. \quad (33)$$

In other words, the second term  $(ii) = \mathcal{F}_k^{h,\Delta} u - \Pi_k^h u$ , which vanishes in  $\Gamma^h$ , is orthogonal to  $\mathcal{D}_0^{0,h}$  with respect to the gradient inner product. Thus its energy norm is a measure of the deviation of  $\Pi_k^h \mathcal{F}_k^{h,\Delta} u$  of being an harmonic function. Since  $\mathbb{P}_m(\mathcal{T}^S) \cap H_0^1(S) \subset \mathcal{D}_0^0(S)$ , for polynomials of arbitrary degree  $m \geq 1$ , the energy norm of the second term (ii) is expected to decay exponentially, and it is eventually dominated by the energy norm of the trace interpolation error represented by the first term (i).

#### 4.4. Examples of SBFEM interpolation errors in a single $S$ -element

Let us consider some examples to illustrate the accuracy capabilities of the SBFEM interpolant, both for smooth or boundary point singularity harmonic functions defined in a single  $S$  element, using refined scaled boundary elements  $\Gamma^{h,S}$ , where uniform Lagrange trace interpolation is adopted.

##### Example 1 - SBFEM interpolation of a smooth harmonic function in 2D

In the region  $S = [-1, 1] \times [-1, 1]$  consider the harmonic function

$$u(x, y) = \exp(\pi x) \sin(\pi y),$$

and interpret  $S$  as polygonal regions of  $4n$  facets,  $n = 2, 4$  and  $8$ , as illustrated in Figure 5. The scaled boundary elements  $\Gamma^{h,S}$  are obtained by subdividing each side of  $\partial S$  into  $n$  subintervals of width  $h = \frac{2}{n}$ . In other words,  $S$  is formed by  $4n$  triangles  $K^e$  sharing the scaling center point as a vertex and having one edge in  $\Gamma^{h,S}$  as an opposite facet. The triangles  $K^e$  are mapped by Duffy's geometric transformations described in Section 2.

For these kinds of scaled geometry, we consider the SBFEM space  $\mathcal{S}_k^{h,S}$ , for  $1 \leq k \leq 4$ , and compute the interpolants  $\Pi_k^{h,S} u$ . The corresponding error histories versus  $h$  are plotted in Figure 6, reflecting the usual convergence behavior governed by the FE trace discretizations  $\mathcal{I}_k^h u$  over  $\partial S$ , of order  $k$  in the energy norm, and order  $k+1$  in the  $L^2$ -norm.

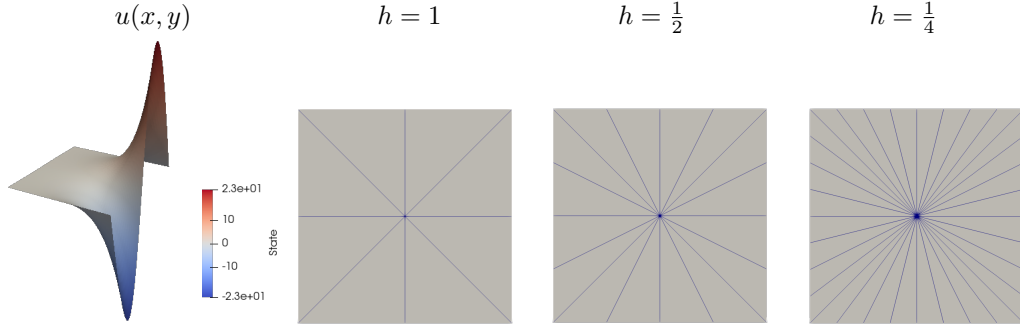


Figure 5: Example 1 - Harmonic function  $u(x, y)$  and scaled triangular partitions  $\mathcal{T}^{h,S}$  of  $S = [-1, 1] \times [-1, 1]$  with scaled boundary  $\Gamma^{h,S}$  formed by  $4n$  uniform facets of width  $h = \frac{2}{n}$ ,  $n = 2, 4$  and  $8$ .

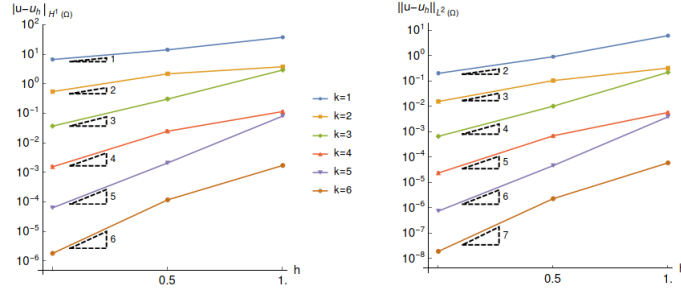


Figure 6: Example 1 - Energy and  $L^2$  SBFEM interpolation errors versus  $h$ :  $\mathbb{S}_k^h(S)$  based on the scaled triangular partitions  $\mathcal{T}^{h,S}$  of Figure 5, and trace spaces  $\Lambda_k^{h,S}$  of degree  $k = 1, \dots, 6$ .

*Example 2 - SBFEM interpolation of a smooth harmonic function in 3D*

The second example is for the harmonic function

$$u(x, y, z) = 4 \left( \exp\left(\frac{\pi x}{4}\right) \sin\left(\frac{\pi y}{4}\right) + \exp\left(\frac{\pi y}{4}\right) \sin\left(\frac{\pi z}{4}\right) \right)$$

defined in the region  $S = [0, 1] \times [0, 1] \times [0, 1]$ . Let SBFEM spaces  $\mathbb{S}_k^{h,S}$  obtained by considering  $S$  as polyhedral regions with  $6n^2$  facets, as illustrated in Figure 14. The scaled boundaries  $\Gamma^{h,S}$  are formed by subdividing each face in  $\partial S$  into  $n \times n$  quadrilaterals, and we set the characteristic size  $h = \frac{1}{n}$ . Thus, the partitions  $\mathcal{T}^{h,S}$  are composed of  $6n^2$  pyramids  $K^e$  sharing the scaling center point as a vertex, which are mapped by Duffy's geometric transformations of the reference hexahedron, as described in Section 2. We

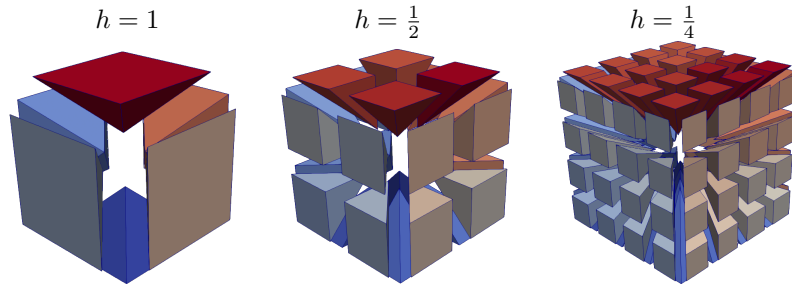


Figure 7: Example 2 - Scaled pyramidal partitions  $\mathcal{T}^{h,S}$  of  $S = [0, 1] \times [0, 1] \times [0, 1]$  with scaled boundary  $\Gamma^{h,S}$  formed by  $6n^2$  uniform quadrilateral facets of characteristic width  $h = \frac{1}{n}$ ,  $n = 1, 2$  and  $4$ .

approximate  $u$  by the SBFEM interpolants  $\Pi_k^{h,S} u$ , and the interpolation error curves are

plotted in Figure 8, revealing the typical optimal convergence rates of order  $k$  in energy norm, and order  $k + 1$  in the  $L^2$  norm of the trace interpolant.

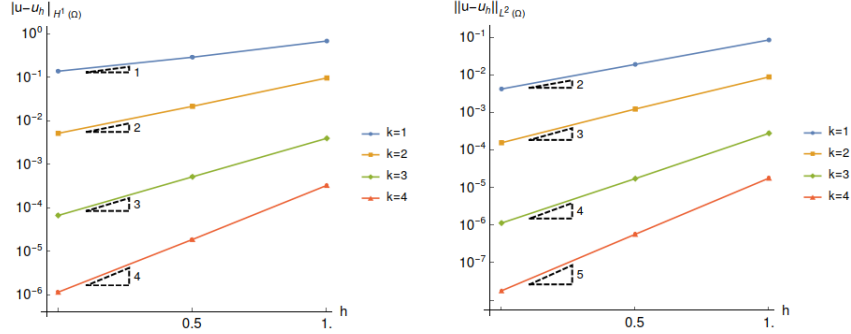


Figure 8: Example 2 - Energy and  $L^2$  SBFEM interpolation errors versus  $h$ :  $\mathbb{S}_k^h(S)$  based on the scaled pyramidal partitions  $\mathcal{T}^{h,S}$  of Figure 7, and trace spaces  $\Lambda_k^{h,S}$  of degree  $k = 1, \dots, 4$ .

### Example 3 - SBFEM interpolation of a singular harmonic function

In the region  $S = [-1, 1] \times [0, 1]$  define the harmonic function

$$u(x, y) = 2^{-1/4} \sqrt{x + \sqrt{x^2 + y^2}} = 2^{1/4} \sqrt{r} \cos\left(\frac{\theta}{2}\right),$$

shown in Figure 9, with a radial square root singularity at the boundary point  $\mathbf{O} = (0, 0)$  ( $r = 0$ ), caused by boundary condition change from Dirichlet  $u(x, 0) = 0$ , for  $x < 0$ , to Neumann  $\partial u / \partial y(x, 0) = 0$ , for  $x > 0$ . This function belongs to  $H^{\frac{3}{2}-\epsilon}(\Omega)$ , for all  $\epsilon > 0$ .

We put the scaling center at the origin and take an open scaled boundary  $\Gamma^{h,S}$  over the two vertical and the top horizontal sides of  $S$ , which are uniformly subdivided:  $n$  uniform intervals for the vertical edges, and  $2n$  for the top edge,  $n = 1, 2$  and  $4$ . This way, in each refinement level,  $S$  is composed of internal triangular partition  $\mathcal{T}^{h,S}$  formed by  $4n$  triangles sharing the scaling center as collapsed vertex, and opposite facet width  $h = \frac{1}{n}$ . Because  $\Gamma^{h,S}$  is not a closed curve, some care must be taken in the construction of the SBFEM space  $\mathbb{S}_k^h(S)$  in order to incorporate boundary data for  $u$  on the bottom boundary side of  $S$ . This is accomplished by enforcing in the second order SBFEM ODE system a vanishing Dirichlet boundary condition on one side (associated with vanishing trace value at  $\mathbf{x}_b = (-1, 0)$ ), whilst a vanishing Neumann condition is assumed on the opposite side (associated with vanishing normal trace at  $\mathbf{x}_b = (1, 0)$ ). These boundary data are radially extended over the sectors  $[-1, 0)$  and  $[0, 1]$ .

SBFEM interpolation errors for this singular example are plotted in Figure 10, revealing usual optimal convergence rates known for trace interpolations by piecewise polynomials. These results reflect the role of the two terms in the decomposition (30), where the dominant contribution is expected to come from the virtual interpolant error, determined exclusively by the trace interpolant, which is not affected by eventual function singularity not interacting with the scaled boundary  $\Gamma^{h,S}$ .

## 5. Galerkin SBFEM approximations

This section is dedicated to the Galerkin SBFEM for the Laplace's model problem

$$\begin{aligned} \Delta u &= 0, \text{ in } \Omega, \\ \gamma_0(u) &= u_D, \text{ on } \partial\Omega, \end{aligned} \tag{34}$$

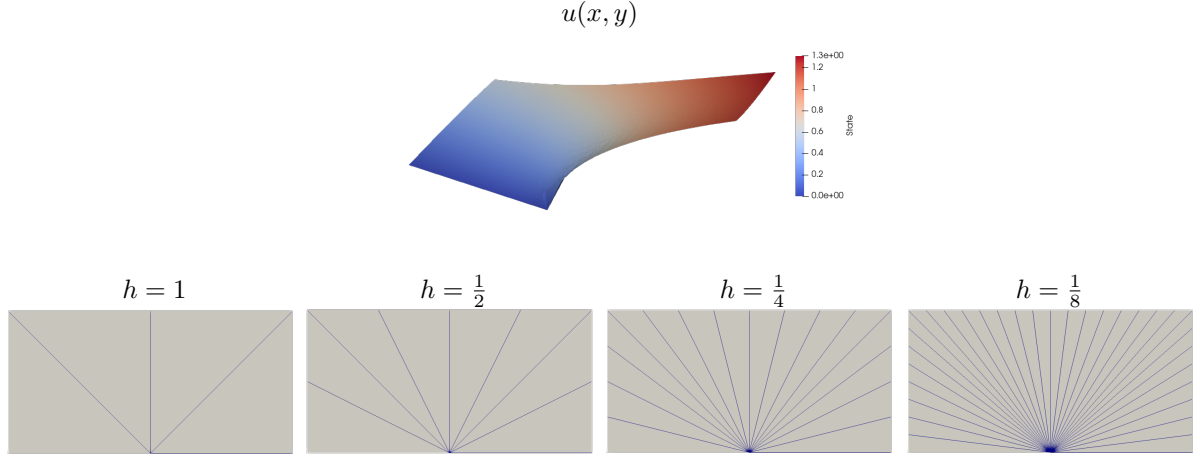


Figure 9: Example 3 - Singular harmonic function  $u(x, y)$  and scaled triangular partitions  $\mathcal{T}^{h,S}$  of  $S = [-1, 1] \times [0, 1]$ , with open scaled boundary  $\Gamma^{h,S}$ , with  $4n$  uniform facets,  $h = \frac{1}{n}$ ,  $n = 1, 2, 4$  and  $8$ .

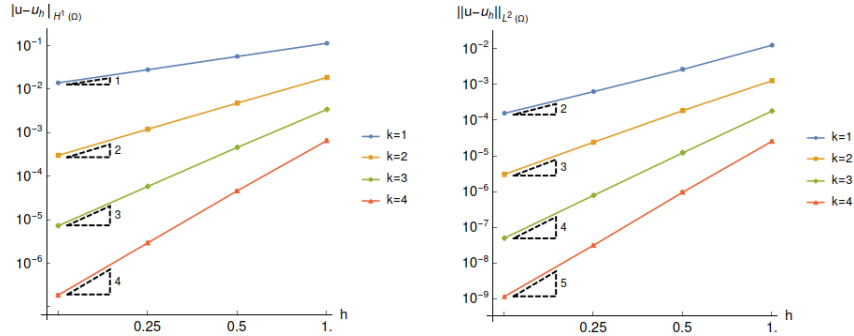


Figure 10: Example 3 - Energy and  $L^2$  SBFEM interpolation errors versus  $h$ :  $\mathbb{S}_k^h(S)$  based on the scaled triangular partitions  $\mathcal{T}^{h,S}$  of Figure 9, and trace spaces  $\Lambda_k^{h,S}$  of degree  $k = 1, \dots, 4$ .

where  $u_D \in H^{1/2}(\partial\Omega)$ , and  $\gamma : H^1(\Omega) \rightarrow H^{1/2}(\partial\Omega)$  is the usual trace operator. We assume that  $u_D$  is sufficiently smooth for the definition of the trace interpolant.

Let  $\mathbb{S}_k^h$  be the trial SBFEM approximation spaces based on geometric partitions  $\mathcal{T}^h = \{S\}$  of  $\Omega$  by  $S$ -elements,  $\Pi_k^h : H^s(\Omega) \rightarrow \mathbb{S}_k^h$  being the corresponding interpolant operators, as defined in the previous section. The Galerkin SBFEM for problem (34) searches approximate solutions  $u^h \in \mathbb{S}_k^h$  satisfying:

$$a(u_h, v) = 0 \quad \forall v \in \mathbb{S}_{k,0}^h, \quad (35)$$

$$u_h|_{\partial\Omega} = \mathcal{I}_k^h u_D|_{\partial\Omega}, \quad (36)$$

where  $a(w, v) := \int_{\Omega} \nabla w \cdot \nabla v \, d\Omega$  is the usual bounded symmetric bilinear form for  $u, w \in H^1(\Omega)$ . The bilinear form  $a$  is well known to be coercive, meaning there exist  $\nu > 0$  such that  $a(v, v) \geq \nu \|v\|_{H^1}^2$ ,  $\forall v \in H_0^1(\Omega)$ . Thus, problem (35)-(36) is well-posed (see [35, Proposition 3.26]).

### 5.1. Error analysis for the SBFEM

For the error analysis of the Galerkin SBFEM discretization (35)-(36), the purpose is to explore the properties (27) and (33) to estimate energy errors  $|u - u^h|_{H^1}$  in approximating the harmonic exact solution  $u$  from the projection errors  $|u - \mathcal{F}_k^{h,FE} u|_{H^1}$  on the FE spaces  $\mathcal{V}_k^{h,FE}$ , or  $|u - \mathcal{F}_k^{h,\nabla} u|_{H^1}$  on the virtual harmonic spaces  $\mathcal{V}_k^{h,\Delta}$ . Recall that the FE

interpolant errors are available in [28, 29, 31, 32] for general functions in Sobolev spaces, whilst interpolant errors  $|u - \mathcal{F}_k^{h,\Delta} u|_{H^1}$  are accessed in [19] for harmonic functions.

**Theorem 5.1.** *Let  $\mathcal{T}^h = \{S\}$  be a family of polygonal partitions of  $\Omega$ ,  $\mathbb{S}_k^h$  be the SBFEM space based on  $\mathcal{T}^h$ , and  $\mathcal{V}_k^{h,FE}$  the FE spaces based on the conglomerate meshes  $\mathcal{P}^h$ . Suppose the same trace interpolant is used in the definitions of  $\Pi_k^h$  and  $\mathcal{F}_k^{h,\Delta}$ , and the exact solution  $u \in H^1$  of the model problem (34) is sufficiently regular for them to make sense. If  $u^h$  or  $\Pi_k^{h,S} u \in \mathbb{S}_k^h$  is the associated Galerkin SBFEM approximation, then*

$$|u - u^h|_{H^1(\Omega)} \leq |u - \mathcal{F}_k^{h,FE} u|_{H^1(\Omega)}. \quad (37)$$

*Proof.* Firstly, we observe two orthogonality relations.

1. As for any Galerkin approximation, the SBFEM solution verify the orthogonality property  $a(u - u^h, v) = 0 \quad \forall v \in \mathbb{S}_{k,0}^h$ , which is paramount for error estimates for such methods.
2. Proposition 4.1 (i.e.,  $\mathcal{F}_k^{h,FE} u \in \mathcal{V}_k^{h,FE} \subset \mathcal{D}_k^h$ ), combined with properties (27) and (26), implies that

$$a(u^h, \Pi_k^h u - \mathcal{F}_k^{h,FE} u) = 0. \quad (38)$$

These two orthogonality relations imply the Pythagorean equality

$$|u - \mathcal{F}_k^{h,FE} u|_{H^1(\Omega)}^2 = |u - u^h|_{H^1}^2 + |u^h - \mathcal{F}_k^{h,FE} u|_{H^1(\Omega)}^2.$$

Consequently, the estimate (37) holds.  $\square$

**Theorem 5.2.** *Let  $\mathcal{T}^h = \{S\}$  be a family of polygonal partitions of  $\Omega$ ,  $\mathbb{S}_k^h$  and  $\mathcal{V}_k^{h,\Delta}$  be the SBFEM and virtual spaces based on  $\mathcal{T}^h$ . Suppose the same trace interpolant is used in the definitions of  $\Pi_k^h$  and  $\mathcal{F}_k^{h,\Delta}$ , and the exact solution  $u \in H^1$  of the model problem (34) is sufficiently regular for them to make sense. If  $u^h \in \mathbb{S}_k^h$  is the associated Galerkin SBFEM approximation, then*

$$|u - u^h|_{H^1(\Omega)} \leq |u - \mathcal{F}_k^{h,\Delta} u|_{H^1(\Omega)} + |\mathcal{F}_k^{h,\Delta} u - \Pi_k^h \mathcal{F}_k^{h,\Delta} u|_{H^1(\Omega)}. \quad (39)$$

*Proof.* The result is a consequence of Galerkin orthogonality property

$$|u - u^h|_{H^1(\Omega)} = \inf_{v \in \mathbb{S}_k^h} |u - v|_{H^1(\Omega)} \leq |u - \Pi_k^h u|_{H^1(\Omega)},$$

the error decomposition (30), and the property  $\Pi_k^h u = \Pi_k^h \mathcal{F}_k^{h,\Delta} u$  remarked in (32).  $\square$

## 6. Numerical experiments

In this section, we present SBFEM simulation results for selected test problems. First, we consider problems with smooth solutions for the verification of the predicted theoretical convergence results of Section 5. For a two-dimensional problem, we explore discretizations based on quadrilateral or polygonal  $S$ -elements subdivided into collapsed scaled triangles. Then, a three-dimensional test problem is explored using SBFEM approximations based on uniform hexahedral and polyhedral  $S$ -elements subdivided into collapsed scaled pyramids, and also on a more general geometry context of polyhedral  $S$ -elements subdivided by scaled collapsed tetrahedra. For comparison, we present results obtained by

$H^1$ -conforming FE methods based on the meshes  $\mathcal{P}^h$  formed by the agglomeration of the corresponding triangles, pyramids, and tetrahedra partitions of the subdomains. Finally, we also evaluate the numerical performance of a coupled FEM+SBFEM formulation for a point singular problem, in which a traditional finite element formulation is modified by a scaled boundary element in the vicinity of the singularity.

For the current simulations, we implemented the method in the computational framework NeoPZ<sup>1</sup>, which is an open source finite element library whose objective is to facilitate the development of innovative technology in finite elements [36]. Such a framework allows using a varied class of element geometries, applying mesh refinement, varying the approximation order, and to approximate partial differential equations using different approximation spaces -  $H^1$ ,  $H(\text{div})$ ,  $H(\text{curl})$  and discontinuous -, as well as mixed and hybrid finite elements and multiscale simulations. As the NeoPZ was conceived using object-oriented concepts, with abstract classes, templates, and small blocks, it offered the required functionalities for a general coding of SBFEM simulations. Moreover, the concept of element neighbours associated with geometric entities in NeoPZ was useful for the construction of the collapsed geometric elements and definition of the scaled boundary partitions. Two and three dimensional SBFEM approximations applied to either Laplace's equation or elasticity are implemented in a single class structure.

*Example 6.1- smooth solution in 2D*

The Laplace equation is approximated on the domain  $\Omega = [-1; 1] \times [-1; 1]$ , where the harmonic problem (34) is considered with exact solution  $u(x, y) = \exp(\pi x) \sin(\pi y)$ . This is the same problem of the interpolation example in Section 4.4, illustrated in Figure 5.

We approximate the problem by the Galerkin SBFEM using sequences of partitions  $\mathcal{T}^h$  for three kinds of  $S$ -elements, with refinement levels  $h = 2^{-\ell}$ ,  $\ell = 1, \dots, 4$ : (i) uniform  $n \times n$ , quadrilateral  $S$ -elements,  $n = 2^{\ell+1}$ , each one having  $\Gamma^S$  formed by its 4 edges, (ii) polygons with 8 edges obtained from uniform quadrilaterals whose sides are subdivided once, and (iii) unstructured polygonal  $S$ -elements constructed using the mesh generator software PolyMesher [37], by giving as input the number of elements in  $x$  and  $y$  axes. For this sequence of four irregular polygonal partitions the scaled boundaries have average characteristic width close to the adopt in the uniform contexts. Thus the same index parameter  $h$  is adopted for them. Recall that each  $S$ -element is subdivided into triangles sharing the scaling center point as a vertex and having one facet in  $\Gamma^{h,S}$  as opposite edge. Figure 11 illustrates the particular partitions for  $h = \frac{1}{4}$ .

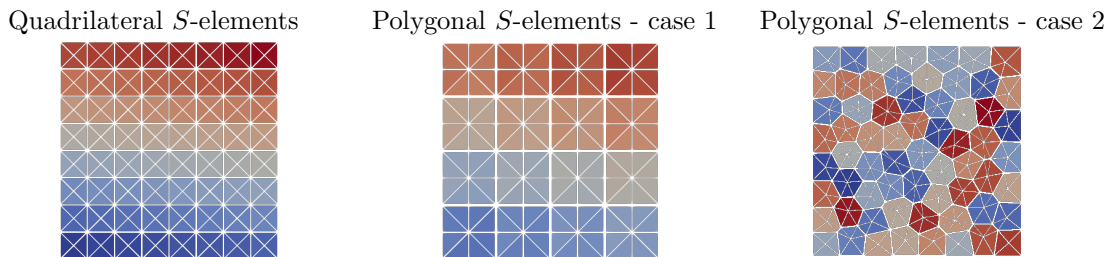


Figure 11: Example 6.1- Uniform quadrilateral and polygonal partitions  $\mathcal{T}^h$ ,  $h = \frac{1}{4}$ :  $S$ -element distinguished by different colors and subdivided into scaled triangles.

<sup>1</sup>NeoPZ open-source platform: <http://github.com/labmec/neoPZ>

Table 1: Example 6.1- Galerkin SBFEM errors  $E_{L^2}^h = \|u - u^h\|_{L^2(\Omega)}$  and  $E_{H^1}^h = |u - u^h|_{H^1(\Omega)}$  for uniform partitions  $\mathcal{T}^h$ ,  $h = 2^{-\ell}$ , of quadrilateral and polygonal (case 1)  $S$ -elements.

Uniform quadrilateral $S$ -elements									
$\ell$	$k=1$			$k=2$			$k=3$		
	DOF	$E_{L^2}^h$	$E_{H^1}^h$	DOF	$E_{L^2}^h$	$E_{H^1}^h$	DOF	$E_{L^2}^h$	$E_{H^1}^h$
1	25	1.80E0	1.99E1	65	1.31E-1	2.56E0	105	7.78E-3	2.28E-1
2	81	4.50E-1	9.50E0	225	1.68E-2	5.92E-1	369	4.68E-4	2.62E-2
3	289	1.13E-1	4.68E0	833	2.12E-3	1.42E-1	1377	2.95E-5	3.19E-3
4	1089	2.82E-2	2.33E0	3201	2.65E-4	3.50E-2	5313	1.86E-6	3.96E-4
	Rate	2.00	1.01	Rate	3.00	2.02	Rate	3.99	3.01
$\ell$	$k=4$			$k=5$			$k=6$		
	DOF	$E_{L^2}^h$	$E_{H^1}^h$	DOF	$E_{L^2}^h$	$E_{H^1}^h$	DOF	$E_{L^2}^h$	$E_{H^1}^h$
1	145	5.87E-4	2.09E-2	185	3.89E-5	1.77E-3	225	1.96E-6	1.03E-4
2	513	1.99E-5	1.29E-3	657	6.04E-7	5.22E-5	801	1.53E-8	1.47E-6
3	1921	6.42E-7	8.14E-5	2465	9.47E-9	1.57E-6	3009	1.23E-10	2.21E-8
4	7425	2.03E-8	5.11E-6	9537	1.48E-10	4.81E-8	11649	9.46E-13	3.42E-10
	Rate	4.98	3.99	Rate	6.00	5.03	Rate	6.99	6.02

Uniform polygonal $S$ -elements - case 1									
$\ell$	$k=1$			$k=2$			$k=3$		
	DOF	$E_{L^2}^h$	$E_{H^1}^h$	DOF	$E_{L^2}^h$	$E_{H^1}^h$	DOF	$E_{L^2}^h$	$E_{H^1}^h$
1	21	8.06E-1	1.23E1	45	8.77E-2	1.95E0	69	8.09E-3	2.53E-1
2	65	2.86E-1	6.66E0	145	1.55E-2	5.30E-1	225	4.98E-4	2.79E-2
3	225	1.54E-2	3.08E0	513	1.87E-3	1.22E-1	801	3.05E-5	3.24E-3
4	833	3.74E-3	1.50E0	1921	2.30E-4	2.97E-2	3009	1.92E-6	3.94E-4
	Rate	2.08	1.04	Rate	3.02	2.04	Rate	3.99	3.02
$\ell$	$k=4$			$k=5$			$k=6$		
	DOF	$E_{L^2}^h$	$E_{H^1}^h$	DOF	$E_{L^2}^h$	$E_{H^1}^h$	DOF	$E_{L^2}^h$	$E_{H^1}^h$
1	93	5.49E-4	2.09E-2	117	3.59E-5	1.70E-3	141	1.78E-6	9.68E-5
2	305	1.98E-5	1.26E-3	385	5.76E-7	4.95E-5	465	1.53E-8	1.44E-6
3	1089	5.99E-7	7.40E-5	1377	8.65E-9	1.41E-6	1665	1.17E-10	2.05E-8
4	4097	1.86E-8	4.54E-6	5185	1.37E-10	4.21E-8	6273	9.03E-13	3.10E-10
	Rate	5.01	4.03	Rate	5.98	5.06	Rate	7.02	6.05

The energy and  $L^2$  errors summarized in Table 1 are for the Galerkin SBFEM solutions in  $\mathbb{S}_k^h$  based on uniform quadrilateral  $S$ -elements and uniform polygonal  $S$ -elements of case 1, using polynomial orders  $1 \leq k \leq 6$ . The numerical results are in accordance with the predicted rates of order  $k$  for energy errors. Optimal rates of order  $k+1$  are also observed for the errors measured by the  $L^2$ -norm.

In Figure 12, the energy and  $L^2$  errors are plotted versus the number of DOF for Galerkin SBFEM solutions in  $\mathbb{S}_k^h$  based on the polygonal meshes of case 2. For comparison, the Galerkin FE solutions in  $\mathcal{V}_k^{h,FE}$  based on the associated scaled triangular partitions  $\mathcal{P}^h$  are also shown, revealing comparable accuracy in both methods, but with less DOF in SBFEM simulations. Recall that SBFEM shape functions are determined by the traces over scaled boundary elements, whilst FE spaces are also populated with shape functions connected with triangular DOF other than the edge ones opposed to the scaling center. One also observe that their error curves approach the possible optimal slopes  $-k$  and  $-(k+1)$  when measured by energy or  $L^2$  norms. This experiment illustrates the SBFEM flexibility with respect to mesh generation for numerical simulations without convergence deterioration.

Plots illustrating SBFEM  $k$ -convergence histories in the energy norm versus DOF are shown in Figure 13, with  $k = 1, \dots, 6$ , and for  $S$ -elements with fixed boundary mesh size  $h = \frac{1}{4}$ . The plots on the left are for the SBFEM interpolation in the single  $S$ -element  $\Omega$  (see Figure 5) and for the Galerkin SBFEM experiment for the uniform quadrilateral partition  $\mathcal{T}^h$  of Figure 11. For both cases, the error decay as  $k$  increases shows a typical

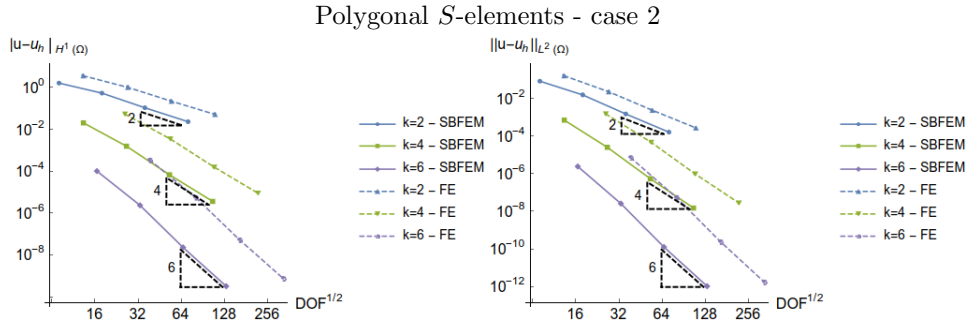


Figure 12: Example 6.1- Energy and  $L^2$  errors versus DOF for the Galerkin SBFEM solutions in  $\mathbb{S}_k^h$ , based on the irregular polygonal  $S$ -elements of case 2 for the Galerkin FE solutions and for the Galerkin FE solutions in  $\mathcal{V}_k^{h,FE}$  based on the associated scaled triangular partitions  $\mathcal{P}^h$ , for  $k = 2, 4$  and  $6$ .

exponential convergence, but the interpolation experiment, by just refining the boundary of a single element, requires less DOF for a given accuracy threshold. For comparison,  $k$ -convergence plots for two  $H^1$ -conforming FE methods are also included: using  $\mathbb{P}_k(K)$  polynomials in the triangles  $K$  of the conglomerate partitions  $\mathcal{P}^h$  (FE), and for Duffy's spaces  $\mathcal{D}_{k,k}^h(S)$  (Duffy's FE). Errors using usual FE and collapsed FE are comparable, but the latter has more equations to be solved. But what is more noticeable on these plots is that SBFEM errors are not only smaller in magnitude than the FE errors (as predicted by Theorem 5.1, since energy FE errors are bounded by FE interpolation errors), but SBFEM requires less DOF to reach a given accuracy, the key property expected to be held for operator adapted methods.

We also compare in Figure 13 (right) the  $k$ -convergence properties of the Galerkin SBFEM for spaces based on  $\mathcal{T}^h$  of the uniform quadrilateral and polygonal  $S$ -elements (case 1) of Figure 11. This comparison experiment shows that the use of the uniform polygonal mesh of case 1 requires fewer equations to be solved for a given target error. On the other hand, a bigger eigenvalue system has to be solved for each  $S$ -element. This kind of polygonal mesh can be seen as a combination of refining both the boundary and inside the subdomains. Due to this flexibility, the SBFEM can generate octree (3D) or quadtree (2D) meshes [15, 38], giving high accuracy, without any additional techniques.

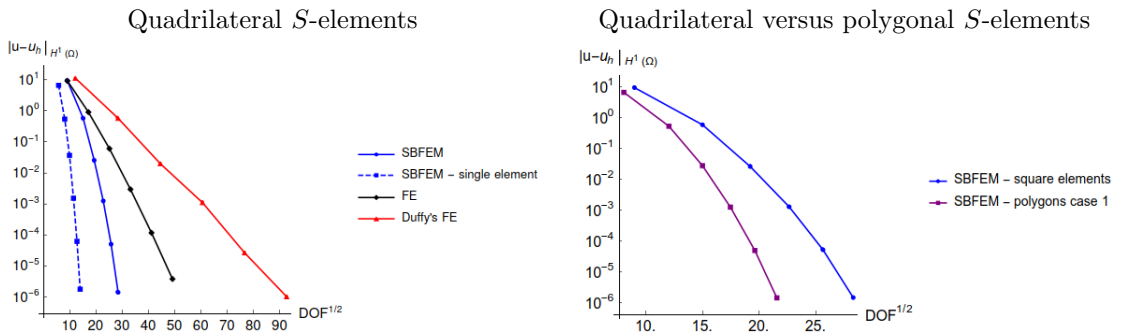


Figure 13: Example 6.1-  $k$ -convergence histories versus the number of DOF, for  $k = 1, \dots, 6$ . Left: SBFEM interpolation  $\Pi_k^{h,S} u$  based on the scaled partition of Figure 5, Galerkin SBFEM for  $\mathbb{S}_k^h$ , Duffy's FE for  $\mathcal{D}_{k,k}^h$ , both based on the uniform quadrilateral partition  $\mathcal{T}^h$  of Figure 11, and FE method for  $\mathcal{V}_k^{h,FE}$  based on the scaled triangular partition  $\mathcal{P}^h$ . Right: Galerkin SBFEM solutions in  $\mathbb{S}_k^h$  using the uniform quadrilaterals and polygonal meshes of case 1 shown in Figure 11. All cases are for  $h = \frac{1}{4}$ .

Section 6.2: smooth solution in 3D

The second example refers to approximating Laplace's equation on a 3D domain  $\Omega = [0, 1] \times [0, 1] \times [0, 1]$ , with exact harmonic solution

$$u(x, y, z) = 4 \left( \exp\left(\frac{\pi x}{4}\right) \sin\left(\frac{\pi y}{4}\right) + \exp\left(\frac{\pi y}{4}\right) \sin\left(\frac{\pi z}{4}\right) \right).$$

This problem corresponds to the interpolation Example 2 of Section 4.4.

Three types of geometry for  $\mathcal{T}^h$  are considered, each one with refinement levels  $h = 2^{-\ell}$ ,  $\ell = 1, 2$ , and 3. The illustrations in Figure 14 are for  $h = \frac{1}{4}$ . One is for  $n \times n \times n$  uniform hexahedral partitions,  $n = 2^\ell$ , where each  $S$ -element is decomposed into six pyramids. The second one is composed of polygons (case 1) constructed by subdividing once each square face of uniform hexahedral partitions into four uniform squares (for this configuration, each  $S$ -element is a polyhedron with 24 quadrilateral facets, and composed by 24 scaled pyramids). More general polyhedral partitions (case 2) are constructed by the software package Neper [39], by giving the number  $n$  of  $S$ -elements in  $x$ ,  $y$ , and  $z$  directions. Then, for each  $S \in \mathcal{T}^h$ , we applied gmsh [40] for the construction of the internal tetrahedral partitions  $\mathcal{T}^{h,S}$ . The average edge characteristic sizes of the scaled boundary elements of these three irregular partitions resulted to be comparable to the parameter  $h$  of the uniform contexts. The pyramids and tetrahedra forming  $S$  are mapped by Duffy's transformations from the reference hexahedron or prism, respectively.

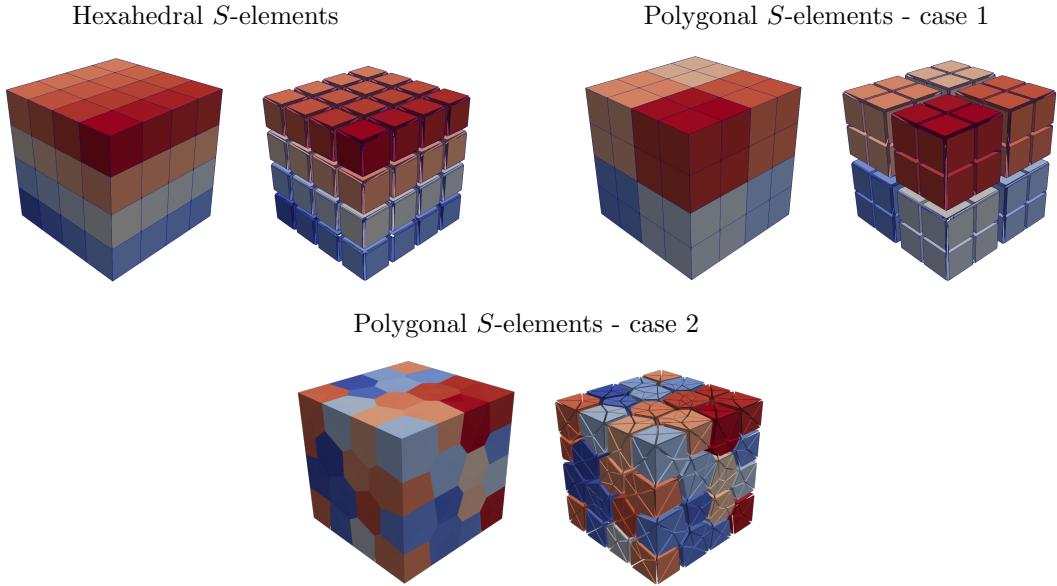


Figure 14: Example 6.2- Hexahedral and polyhedral partitions  $\mathcal{T}^h$ ,  $h = \frac{1}{4}$ :  $\mathcal{T}^{h,S}$  composed by scaled pyramids (top), and by scaled tetrahedra (bottom).

The results for the Galerkin SBFEM solutions in  $\mathbb{S}_k^h$ , with  $k = 1, \dots, 4$ , based on the uniform hexahedral  $S$ -elements and on the polyhedral  $S$ -elements of case 1 are documented in Table 2. Optimal accuracy of order  $k$  for energy norm, and  $k+1$  for the  $L^2$ -norm occur. Energy and  $L^2$  errors obtained with the polyhedral partitions of case 2 are plotted versus DOF in Figure 15. For comparison, the Galerkin FE solutions in  $\mathcal{V}_k^{h,FE}$  based on the associated scaled tetrahedral partitions  $\mathcal{P}^h$  are also shown. Similar conclusions hold as for the experiment shown in Figure 12. One can also observe that both Galerkin SBFEM and FE approximation errors have similar magnitude, but with less DOF in the SBFEM

Table 2: Example 6.2- Galerkin SBFEM errors  $E_{L^2}^h = \|u - u^h\|_{L^2(\Omega)}$  and  $E_{H^1}^h = \|u - u^h\|_{H^1(\Omega)}$  for uniform partitions  $\mathcal{T}^h$  of hexahedral and polyhedral (case 1)  $S$ -elements, with  $h = 2^{-\ell}$ .

Uniform hexahedral $S$ -elements												
$\ell$	$k=1$			$k=2$			$k=3$			$k=4$		
	DOF	$E_{L^2}^h$	$E_{H^1}^h$									
1	27	3.17E-2	3.85E-1	117	1.41E-3	2.40E-2	279	1.92E-5	5.22E-4	513	6.46E-7	2.09E-5
2	127	7.85E-3	1.87E-1	665	1.93E-4	6.02E-3	1685	1.25E-6	6.49E-5	3185	2.12E-8	1.31E-6
3	729	1.93E-3	9.20E-2	4401	2.48E-5	1.51E-3	11529	7.99E-8	8.07E-6	22113	6.75E-10	8.16E-8
	Rate	2.03	1.02	Rate	2.96	2.00	Rate	3.97	3.01	Rate	4.98	4.00

Uniform polyhedral $S$ -elements - case 1												
$\ell$	$k=1$			$k=2$			$k=3$			$k=4$		
	DOF	$E_{L^2}^h$	$E_{H^1}^h$									
1	26	1.94E-2	2.96E-1	98	1.25E-3	2.21E-2	218	1.76E-5	5.30E-4	386	5.83E-7	1.92E-5
2	117	5.24E-3	1.42E-1	513	1.68E-4	5.34E-3	1197	1.19E-6	6.45E-5	2169	1.91E-8	1.18E-6
3	665	1.35E-3	7.00E-2	3185	2.14E-5	1.33E-3	7625	7.79E-8	7.92E-6	13985	6.08E-10	7.32E-8
	Rate	1.96	1.02	Rate	2.97	2.01	Rate	3.93	3.03	Rate	4.97	4.01

systems. Their error curves measured with energy and  $L^2$  norms also approach the possible optimal slopes  $-k$  and  $-(k+1)$ , respectively.

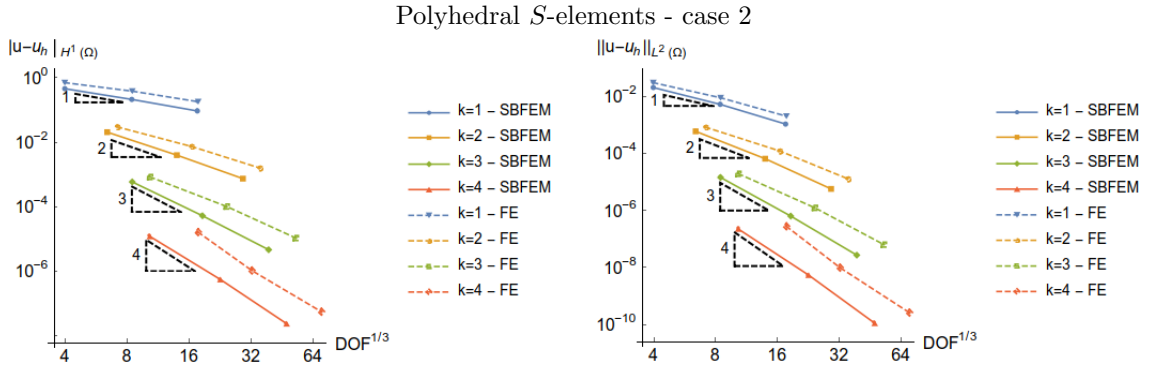


Figure 15: Example 6.2- Energy and  $L^2$  errors versus DOF for the Galerkin SBFEM solution in  $\mathbb{S}_k^h$ , for  $k = 1, \dots, 4$ , based on the irregular polyhedral  $S$ -elements of case 2.

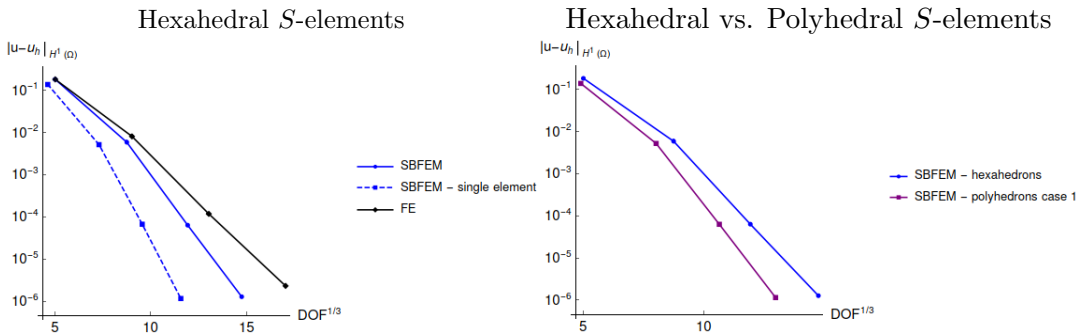


Figure 16: Example 6.2-  $k$ -convergence histories as function of the number of DOF, for  $k = 1, \dots, 4$ : Left: SBFEM interpolation  $\Pi_k^{h,S} u$  for the scaled partition  $\mathcal{T}^{h,S}$  of Figure 7, Galerkin SBFEM for  $\mathbb{S}_k^h$  based on uniform hexahedral partition  $\mathcal{T}^h$ , and FE method for  $\mathcal{V}_k^{h,FE}$  based on the conglomerated scaled pyramidal partition  $\mathcal{P}^h$ . Right: Galerkin SBFEM for  $\mathbb{S}_k^h$  based on hexahedral and polyhedral  $S$ -elements of case 1. In all the experiments,  $h = \frac{1}{4}$ .

In the left side of Figure 16, we compare the SBFEM  $k$ -convergence using the fixed

uniform hexahedral partition at the refinement level  $h = \frac{1}{4}$ , shown in Figure 14, with equivalent results for the FE method using the spaces  $\mathcal{V}_k^{h,FE} \subset H^1(\Omega)$  based on the associated pyramidal partition  $\mathcal{P}^h$ . SBFEM approximations lead to lower error values, as predicted by Theorem 5.1, and the linear systems have a reduced number of equations. The error curve of the interpolation experiment illustrated in Figure 8 is also included.

The plots on the right side compare the  $k$ -convergence of the two SBFEM solutions in  $\mathbb{S}_k^h$  based on the uniform hexahedral partition and on the polyhedral partition of case 1 illustrated in Figure 14, both with  $h = \frac{1}{4}$ . Similarly to the comparison experiment of the previous example, shown in Figure 13, these convergence histories also show that the use of polygonal mesh requires fewer equations to be solved for a given target error, but reminding that it requires bigger eigenvalue systems to be solved for the computation of SBFEM shape functions in the  $S$ -elements.

### Section 6.3: coupled FE-SBFEM formulation for a singular problem

Taking the singular harmonic function interpolated in Section 4.4, namely

$$u = 2^{1/4} \sqrt{r} \cos\left(\frac{\theta}{2}\right) = 2^{-1/4} \sqrt{x + \sqrt{x^2 + y^2}},$$

we enforce Dirichlet boundary condition on  $(x, 0)$ ,  $x < 0$ , and Neumann boundary condition elsewhere. Due to the lack of regularity of  $u \in H^{\frac{3}{2}-\epsilon}(\Omega)$ , the error estimates of Theorem 5.1 in terms of FE interpolant error based on regular partitions are restricted in theory to order  $h^{\frac{1}{2}-\epsilon}$ . This problem was considered in [41] to evaluate the efficiency of the mixed FE method when quarter-point elements are used in the vicinity of the origin  $\mathbf{O} = (0, 0)$  (singular point), showing dramatic accuracy improvement. Recall that the specific 6-noded quarter-point element is also of Duffy's type, obtained by collapsing a reference quadrilateral element on triangles.

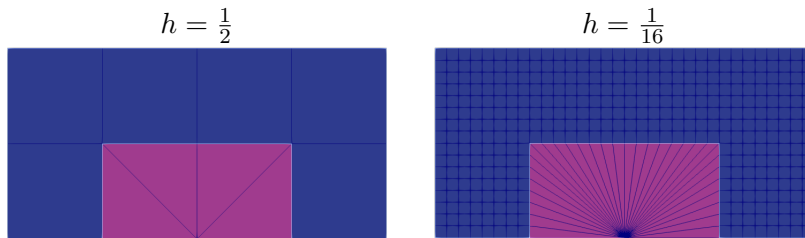


Figure 17: Example 6.3- Meshes for the coupled FE-SBFEM formulation: FE (blue) in the smooth region and SBFEM (magenta) close to the singularity point.

With this motivation, we propose a formulation composing SBFEM approximations in a single element  $S = [-0.5, 0.5] \times [0, 0.5]$  and FE approximations elsewhere, in the region where the solution is smooth. Similarly to the interpolation experiments in Section 4.4, the space  $\mathbb{S}_k^h(S)$  is conceived in such a way that the scaling center is located on the singularity point, which means that an open scaled boundary element is applied. The vertical and top-horizontal edges of  $S$  are uniformly subdivided to form an interface partition  $\Gamma^{h,S}$ . Elsewhere, a uniform quadrilateral mesh matching  $\Gamma^{h,S}$  is adopted, as illustrated in Fig 17 for  $h = \frac{1}{2}$  and  $h = \frac{1}{16}$ . The coupling between FE and SBFEM approximations is straightforward since SBFEM uses compatible FE spaces at the interface. Four mesh sizes  $h = 2^{-\ell}$ ,  $\ell = 1, \dots, 4$ , and polynomials of degree  $k = 1, \dots, 4$  are performed.

The corresponding results are documented in Table 3. As for regular problems with smooth solutions, optimal rates of convergence of order  $k$  and  $k + 1$  for energy and  $L^2$  errors hold for this singular problem, without any adaptivity, i.e. uniform degree  $k$  is used over the domain and no  $h$ -adaptivity is applied as well.

Table 3: Example 6.3- Errors  $E_{L^2}^h = \|u - u^h\|_{L^2(\Omega)}$  and  $E_{H^1}^h = |u - u^h|_{H^1(\Omega)}$ ,  $h = 2^{-\ell}$ , for the combined FE-SBFEM method.

$\ell$	$k=1$			$k=2$			$k=3$			$k=4$		
	DOF	$E_{L^2}^h$	$E_{H^1}^h$									
1	14	8.44E-4	1.11E-1	26	7.87E-4	1.94E-2	76	9.17E-5	2.82E-3	125	1.19E-5	5.25E-4
2	39	2.02E-3	5.54E-2	117	1.12E-4	4.23E-3	259	6.35E-6	3.83E-4	441	4.59E-7	3.72E-5
3	125	4.95E-4	2.73E-2	665	1.45E-5	1.06E-3	949	4.16E-7	4.87E-5	1649	1.54E-8	2.39E-6
4	441	1.23E-4	1.36E-2	4401	1.84E-6	2.66E-4	3625	2.67E-8	6.10E-6	6369	4.97E-10	1.50E-7
	Rate	2.01	1.01	Rate	2.99	2.00	Rate	3.96	3.00	Rate	4.96	3.99

For comparison, two  $k$ -convergence histories as function of the number of DOF are shown in Figure 18 for fixed partitions of the domain  $\Omega$ : one for the SBFEM interpolation errors computed in Example 3, Section 4.4, and the other for the combined Galerkin FE-SBFEM method. The partitions used in these experiments are illustrated in Figure 18, noticing that they coincide within the region  $S$  around the singularity, but the FE partition in the smooth region being more refined. Whilst SBFEM interpolation in the single element  $\Omega$  requires much less DOF, both experiments reach very close error values, because the error in this problem is governed by the singularity, modeled using SBFEM in both experiments. However, the results of Fig 18 could be deceiving. It should be emphasized that global SBFEM interpolation in the whole domain  $\Omega$  was feasible in this particular test problem, but this will not be the case in practical singular problems, for which coupled FE+SBFEM simulations reveal to be a simple and efficient option.

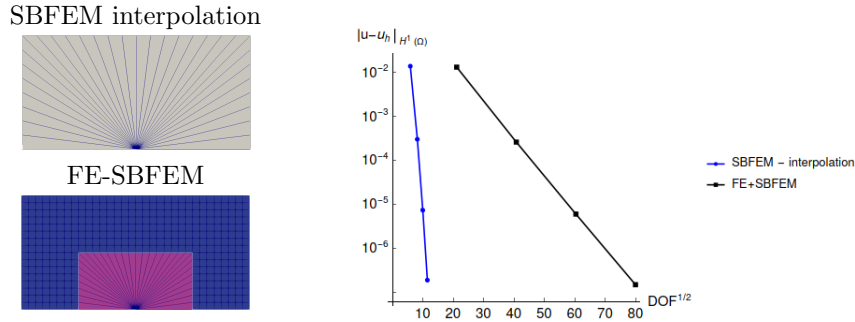


Figure 18: Example 6.3- Partitions and  $k$ -convergence histories versus the number of DOF, with  $k = 1, \dots, 4$ , for SBFEM interpolants  $\Pi^{h,S} u$  of Example 3, Section 4.4, and Galerkin FE-SBFEM solutions.

## 7. Conclusions

We provide a priori error estimates in energy norm for Galerkin SBFEM approximations of harmonic solutions by exploring two aspects of SBFEM's methodology.

The SBFEM approximation spaces are based on star-shaped polytopal subregions ( $S$ -elements), where the functions are parametrized in the radial and surface directions. We show that they can be presented in the context of Duffy's approximations based on subpartitions of the  $S$ -elements. Piecewise polynomial discretization is adopted for surface

traces, which are radially extended to the interior of  $S$  by solving local harmonic problems using test functions restricted to Duffy's spaces. As a consequence, shape functions can be derived from analytical solutions defined by eigenvalue problems, whose coefficients are determined by the geometry of the  $S$ -elements.

We demonstrate that there is an equivalence between the SBFEM ODE equation and an orthogonality property of SBFEM spaces, with respect to the gradient inner product for a wide class of Duffy's approximations vanishing on the facets of  $S$ . This orthogonal property is the key for the derivation of the estimation of SBFEM errors in energy norm. The Galerkin SBFEM approximation error is necessarily smaller than the FE interpolant error for the FE space included in the Duffy's space sharing the same interface traces.

We show that SBFEM errors in the approximation of harmonic functions come from two sources: there is the kind of error caused when the trace of harmonic functions are discretized over the facets of  $S$ , occurring in virtual harmonic approximations, and there is the error caused by the deviation of SBFEM approximations of being harmonic inside  $S$ . The fact that the first source of error is the dominant one is favorable for applications for singular problems, where the singularity may be isolated, without interaction with the  $S$ -element facets. For this class of problems, the solution away from the singularity is regular. If the convergence rate is dominated by the approximation on the boundary of  $S$ , then this explains regular convergence rates even for singular problems, as illustrated by the verification simulations.

Numerical tests in 2D and 3D problems emphasize the optimal rate of convergence of the scaled boundary approximations, proven theoretically for the energy norm. Although we have considered only harmonic solutions, the demonstration can be extended for more general homogeneous elliptic PDEs, for instance, elasticity problems without body loads.

## Acknowledgements

The authors thankfully acknowledge financial support from: FAPESP - São Paulo Research Foundation, grants 2016/05155-0 (Gomes) and 17/08683-0 (Devloo), CNPq - Conselho Nacional de Desenvolvimento Científico e Tecnológico, grants 305823-2017-5 (Devloo) and 306167/2017-4 (Gomes), and ANP - Brazilian National Agency of Petroleum, Natural Gas and Biofuels, grant 2014/00090-2 (Coelho, Devloo).

## References

- [1] C. Song, J. P. Wolf, The scaled boundary finite-element method—alias consistent infinitesimal finite-element cell method—for elastodynamics, *Computer Methods in Applied Mechanics and Engineering* 147 (1997) 329–355.
- [2] C. Song, J. P. Wolf, The scaled boundary finite-element method: analytical solution in frequency domain, *Computer Methods in Applied Mechanics and Engineering* 164 (1998) 249–264.
- [3] J. P. Wolf, *The Scaled Boundary Finite Element Method*, John Wiley & Sons, 2003.
- [4] C. Song, *The Scaled Boundary Finite Element Method: Theory and Implementation*, John Wiley & Sons, 2018.
- [5] I. Babuška, J. M. Melenk, The partition of unity method, *International Journal for Numerical Methods in Engineering* 40 (1997) 727–758.

- [6] J. M. Melenk, Operator Adapted Spectral Element Methods I: Harmonic and Generalized Harmonic Polynomials, *Numerische Mathematik* 1 (1999) 35–69.
- [7] Z. Yang, Fully automatic modelling of mixed-mode crack propagation using scaled boundary finite element method, *Engineering Fracture Mechanics* 73 (2006) 1711–1731.
- [8] C. Song, E. T. Ooi, S. Natarajan, A review of the scaled boundary finite element method for two-dimensional linear elastic fracture mechanics, *Engineering Fracture Mechanics* 187 (2018) 45–73.
- [9] A. L. N. Pramod, R. K. Annabattula, E. T. Ooi, C. Song, S. Natarajan, Others, Adaptive phase-field modeling of brittle fracture using the scaled boundary finite element method, *Computer Methods in Applied Mechanics and Engineering* 355 (2019) 284–307.
- [10] H. Guo, E. T. Ooi, A. A. Saputra, Z. Yang, S. Natarajan, E. H. Ooi, C. Song, A quadtree-polygon-based scaled boundary finite element method for image-based mesoscale fracture modelling in concrete, *Engineering Fracture Mechanics* 211 (2019) 420–441.
- [11] J. Bulling, H. Gravenkamp, C. Birk, A high-order finite element technique with automatic treatment of stress singularities by semi-analytical enrichment, *Computer Methods in Applied Mechanics and Engineering* 355 (2019) 135–156.
- [12] Y. Liu, A. A. Saputra, J. Wang, F. Tin-Loi, C. Song, Automatic polyhedral mesh generation and scaled boundary finite element analysis of STL models, *Computer Methods in Applied Mechanics and Engineering* 313 (2017) 106–132.
- [13] S. Natarajan, P. Dharmadhikari, R. K. Annabattula, J. Zhang, E. T. Ooi, C. Song, Extension of the scaled boundary finite element method to treat implicitly defined interfaces without enrichment, *Computers & Structures* 229 (2020) 106–159.
- [14] A. Saputra, H. Talebi, D. Tran, C. Birk, C. Song, Automatic image-based stress analysis by the scaled boundary finite element method, *International Journal for Numerical Methods in Engineering* 109 (2017) 697–738.
- [15] K. Chen, D. Zou, X. Kong, X. Yu, An efficient nonlinear octree SBFEM and its application to complicated geotechnical structures, *Computers and Geotechnics* 96 (2018) 226–245.
- [16] H. Gravenkamp, A. A. Saputra, S. Duczek, High-order shape functions in the scaled boundary finite element method revisited, *Archives of Computational Methods in Engineering* (2019) 1–22.
- [17] H. Gravenkamp, A. A. Saputra, S. Eisenträger, Three-dimensional image-based modeling by combining SBFEM and transfinite element shape functions, *Computational Mechanics* (2020) 1–20.
- [18] M. G. Duffy, Quadrature over a pyramid or cube of integrands with a singularity at a vertex, *SIAM Journal on Numerical Analysis* 19 (1982) 1260–1262.

- [19] A. Chernov, L. Mascotto, The harmonic virtual element method: stabilization and exponential convergence for the Laplace problem on polygonal domains, *IMA Journal of Numerical Analysis*, 39(4), 1787-1817 33 (2019) 1787–1817.
- [20] J. N. Lyness, R. Cools, A survey of numerical cubature over triangles, Technical Report, Argonne National Laboratory, 1994.
- [21] M. G. Blyth, C. Pozrikidis, A Lobatto interpolation grid over triangle, *IMA Journal of Applied Mathematics* 71 (2006) 153–169.
- [22] G. Karniadakis, S. Sherwin, *Spectral/hp Element Methods for Computational Fluid Dynamics*, Oxford University Press, 1999.
- [23] Y.-L. Wu, Collapsed isoparametric element as a singular element for a crack normal to the bi-material interface, *Computers & Structures* 47 (1993) 939–943.
- [24] S. L. Pu, M. Hussain, W. E. Lorensen, The collapsed cubic isoparametric element as a singular element for crack problems, *International Journal for Numerical Methods in Engineering* 12 (1978) 1727–1742.
- [25] I. S. Raju, Calculation of strain-energy release rates with higher order and singular finite elements, *Engineering Fracture Mechanics* 28 (1987) 251–274.
- [26] J. Shen, L.-L. Wang, H. Li, A Triangular Spectral Element Method Using Fully Tensorial Rational Basis Functions, *SIAM Journal on Numerical Analysis* 47 (2008) 1619–1650.
- [27] N. Nigam, J. Phillips, High-order conforming finite elements on pyramids, *IMA Journal of Numerical Analysis* 32 (2012) 448–483.
- [28] I. Babuška, M. Suri, The h-p version of the finite element method with quasiuniform meshes, *RAIRO - Modélisation Mathématique et Analyse Numérique* 21 (1987) 199–238.
- [29] R. Muñoz-Sola, Polynomial lifting on the tetrahedron and applications to the h-p version of the finite element method in three dimensions, *SIAM Journal on Numerical Analysis* 34 (1997) 282–314.
- [30] L. Demkowicz, Polynomial Exact Sequences and Projection-Based Interpolation with Application to Maxwell Equations, in: D. Boffi, L. Gastaldi (Eds.), *Mixed Finite Elements, Compatibility Conditions, and Applications*, Lecture Notes in Mathematics, Vol. 1939, Springer, 2008, pp. 101–158.
- [31] L. Demkowicz, J. Kurtz, D. Pardo, M. Paszynski, W. Rachowicz, A. Zdunek, *Computing with hp-Adaptive Finite Elements*, Vol. 2, Chapman and Hall, 2007.
- [32] J. M. Melenk, C. Rojik, On commuting p-version projection-based interpolation on tetrahedra, *Mathematics of Computation* 89 (2020) 45–87.
- [33] M. Bergot, G. Cohen, M. Duriflé, Higher-order finite elements for hybrid meshes using new nodal pyramidal elements, *Journal of Scientific Computing* 42 (2010) 345–381.

- [34] C. Schwab, p-and hp-Finite Element Methods: Theory and Applications in Solid and Fluid Mechanics, Clarendon Press Oxford, 1998.
- [35] A. Ern, J.-L. Guermond, Theory and Practice of Finite Elements, Vol. 159, Springer Science & Business Media, 2013.
- [36] P. R. B. Devloo, PZ: An object oriented environment for scientific programming, Computer Methods in Applied Mechanics and Engineering 150 (1997) 133–153.
- [37] C. Talischi, G. H. Paulino, A. Pereira, I. F. M. Menezes, PolyMesher: a general-purpose mesh generator for polygonal elements written in Matlab, Structural and Multidisciplinary Optimization 45 (2012) 309–328.
- [38] A. A. Saputra, S. Eisenträger, H. Gravenkamp, C. Song, Three-dimensional image-based numerical homogenisation using octree meshes, Computers & Structures 237 (2020) 106263.
- [39] R. Quey, P. R. Dawson, F. Barbe, Large-scale 3D random polycrystals for the finite element method: Generation, meshing and remeshing, Computer Methods in Applied Mechanics and Engineering 200 (2011) 1729–1745.
- [40] C. Geuzaine, J.-F. Remacle, Gmsh: A 3-D finite element mesh generator with built-in pre-and post-processing facilities, International Journal for Numerical Methods in Engineering 79 (2009) 1309–1331.
- [41] D. de Siqueira, A. M. Farias, P. R. B. Devloo, S. M. Gomes, Mixed finite element approximations of a singular elliptic problem based on some anisotropic and hp-adaptive curved quarter-point elements, Applied Numerical Mathematics 158 (2020) 85–102.

## Appendix A. Scaled ODE equation

The second-order ODE problem (15) can be solved using standard methods through a system of first-order differential equations. Given  $\hat{\underline{Q}}_i(\xi) = \left[ \xi^{d-1} \underline{E}_{11} \hat{\underline{\Phi}}_i'(\xi) + \xi^{d-2} \underline{E}_{21} \hat{\underline{\Phi}}_i(\xi) \right]$ , the ODE (15) can be expressed by the two equations:

$$\xi \hat{\underline{\Phi}}_i'(\xi) = \left( -\underline{E}_{11}^{-1} \underline{E}_{12} + 0.5(d-2)\mathbf{I} \right) \hat{\underline{\Phi}}_i(\xi) + \underline{E}_{11}^{-1} \hat{\underline{Q}}_i(\xi), \quad (\text{A.1})$$

$$\xi \hat{\underline{Q}}_i'(\xi) = \left( -\underline{E}_{21} \underline{E}_{11}^{-1} \underline{E}_{12} + \underline{E}_{22} \right) \hat{\underline{\Phi}}_i(\xi) + \left( \underline{E}_{11} \underline{E}_{21}^{-1} - 0.5(d-2)\mathbf{I} \right) \hat{\underline{Q}}_i(\xi). \quad (\text{A.2})$$

This ODE system can be grouped in a matrix form as

$$\xi \underline{\underline{X}}'(\xi) = -\underline{\underline{Z}} \underline{\underline{X}}(\xi), \quad \xi \in [-1, 1], \quad (\text{A.3})$$

for  $\underline{\underline{X}}(\xi) = \begin{bmatrix} \hat{\underline{\Phi}}_i(\xi) \\ \hat{\underline{Q}}_i(\xi) \end{bmatrix}$ , where  $\hat{\underline{\Phi}}_i(\xi) = [\hat{\underline{\Phi}}_i(\xi)]$ , and  $\hat{\underline{Q}}_i(\xi) = [\hat{\underline{Q}}_i(\xi)]$  are  $\mathcal{N}^S \times \mathcal{N}^S$  matrices with columns  $\hat{\underline{\Phi}}_i(\xi)$  and  $\hat{\underline{Q}}_i(\xi)$ , and  $\underline{\underline{Z}}$  is the  $2\mathcal{N}^S \times 2\mathcal{N}^S$  matrix

$$\underline{\underline{Z}} = \begin{bmatrix} \left( \underline{E}_{11}^{-1} \underline{E}_{12} - 0.5(d-2)\mathbf{I} \right) & -\underline{E}_{11}^{-1} \\ -\underline{E}_{22} + \underline{E}_{21} \underline{E}_{11}^{-1} \underline{E}_{21} & \left( -\underline{E}_{21} \underline{E}_{11}^{-1} + 0.5(d-2)\mathbf{I} \right) \end{bmatrix}.$$

If  $\begin{bmatrix} \underline{A} \\ \underline{Q} \end{bmatrix}$  are linearly independent eigenvectors of the matrix  $\underline{Z}$  corresponding to eigenvalues  $\underline{\lambda}$ ,

then the function  $\underline{X}(\xi) = \begin{bmatrix} \underline{A} \\ \underline{Q} \end{bmatrix} \xi^{\underline{\lambda}}$  solves (A.3). The functions  $\xi^{\underline{\lambda}}$  corresponding to eigenvalues having negative real parts are unbounded for  $\xi \rightarrow 0$ , and are unsuited to describe solutions at the interior of the S-element, whilst those of positive real parts represent solutions that are zero at the scaling center of  $S$ . Thus, the desired solutions of the system (A.1)-(A.2) are taken as

$$\hat{\underline{\Phi}}(\xi) = \underline{A}_+ \text{diag}(\xi^{\underline{\lambda}_+}), \quad \hat{\underline{Q}}(\xi) = \underline{Q}_+ \text{diag}(\xi^{\underline{\lambda}_+}),$$

where  $\underline{\lambda}_+ \in \mathbb{R}^N$  represents the positive real part of  $\underline{\lambda}$ ,  $\underline{A}_+ = [\underline{A}_{+i}]$  and  $\underline{Q}_+ = [\underline{Q}_{+i}]$  are the associated eigenvector components. For simplicity, the index  $+$  is dropped in Section 3.3.